

1 ~~A novel spectroscopic approach and sampling method~~ Using 2 Tunable Infrared Laser Direct Absorption Spectroscopy for 3 ambient hydrogen chloride detection: HCl-TILDAS

4 John W. Halfacre¹, Jordan Stewart¹, Scott C. Herndon², Joseph R. Roscioli², Christoph Dyroff²,
 5 Tara I. Yacovitch², Michael Flynn³, Stephen J. Andrews¹, Steven S. Brown^{4,5}, Patrick R.
 6 Veres⁴, Pete M. Edwards¹

7 ¹Wolfson Atmospheric Chemistry Laboratories, Department of Chemistry, University of York, Heslington,
 8 York, YO10 5DD, UK

9 ²Aerodyne Research, Inc., Billerica, MA, 01821, USA

10 ³Department of Earth and Environmental Science, Centre for Atmospheric Science, School of Natural Sciences,
 11 The University of Manchester, Manchester M13 9PL, UK

12 ⁴Chemical Sciences Laboratory, National Oceanic and Atmospheric Administration, Boulder, CO, 80305, USA

13 ⁵Department of Chemistry, University of Colorado, Boulder, CO 80309, USA

14 *Correspondence to:* John Halfacre (john.halfacre@york.ac.uk), Pete Edwards (pete.edwards@york.ac.uk)

15 **Abstract.** The largest inorganic, gas phase reservoir of chlorine atoms in the atmosphere is hydrogen chloride
 16 (HCl), but the challenges in quantitative sampling of this compound cause difficulties for obtaining high-quality,
 17 high-frequency measurements. In this work, tunable infrared laser direct absorption spectroscopy (TILDAS) was
 18 demonstrated to be a superior optical method for sensitive, in situ detection of HCl at the 2925.89645 cm⁻¹
 19 absorption line using a 3 μm interband cascade laser. The instrument has an effective path length of 204 m, 1 Hz
 20 precision of 7-8 pptv, and 3σ limit of detection ranging from 21-24 pptv. For longer averaging times, the highest
 21 precision obtained was 0.5 pptv and 3σ limit of detection of 1.6 pptv at 2.4 minutes. HCl TILDAS was also shown
 22 to have high accuracy when compared with a certified gas cylinder, yielding a linear slope within the expected
 23 5% tolerance of the reported cylinder concentration (slope = 0.964 ± 0.008). The use of heated inlet lines and
 24 active chemical passivation greatly improve the instrument response times to changes in HCl mixing ratios, with
 25 minimum 90% response times ranging from 1.2 - 4.4 s, depending on inlet flow rate. However, these response
 26 times lengthened at relative humidities > 50%, conditions under which HCl concentration standards were found
 27 to elicit a significantly lower response (-5.8%). The addition of high concentrations of gas phase nitric acid (>
 28 43.0 ppbv) were found to increase HCl signal (< 10%), likely due to acid displacement with HCl or particulate
 29 chloride adsorbed to inlet surfaces. The equilibrium model ISORROPIA suggested a potential of particulate
 30 chloride partitioning into HCl gas within the heated inlet system if allowed to thermally equilibrate, but field
 31 results did not demonstrate a clear relationship between particulate chloride and HCl signal obtained with a
 32 denuder installed on the inlet.

33 1 Introduction

34 Growing attention is being given to the role of reactive chlorine in tropospheric oxidation chemistry (Simpson et
 35 al., 2015), given its potential impacts on the lifetimes of volatile organic compounds; atomic chlorine reacts with
 36 hydrocarbons at rate constants often orders of magnitude greater than those with hydroxyl radical (Burkholder et
 37 al., 2015; Atkinson et al., 2006; Jahn et al., 2021), as in Reaction (R1), where R represents an alkane:



40
 41 Even moderate amounts of such a potent oxidizer could lead to changes in concentrations of O₃, NO_x, and hydroxyl
 42 radicals. However, the high reactivity of atomic chlorine radicals, combined with a lack of effective gas phase
 43 recycling mechanisms, only allows for a small degree of accumulation, with global tropospheric averages
 44 estimated to range between 10²-10⁵ atoms cm⁻³ (Allan et al., 2001; Pszenny et al., 2007; Wang et al., 2021;
 45 Wingenter et al., 1996; Singh et al., 1996). As such, in situ, quantitative detection of atomic chlorine radicals
 46 remains out of reach. It is instead more practical to study chlorine through relatively more abundant and stable
 47 reservoir species, such as hydrogen chloride (e.g., Angelucci et al., 2021), molecular chlorine (e.g., Liao et al.,
 48 2014), chlorine monoxide (e.g., Tuckermann et al., 1997), and nitryl chloride (e.g., Osthoff et al., 2008).

49 Hydrogen chloride (HCl) is of particular interest because it is the most abundant form of inorganic
 50 chlorine in the gas phase and acts as both a source and end-product of atomic chlorine. Reaction (R1) represents
 51 a significant gas phase HCl formation pathway, but its largest atmospheric source on a global basis is sea salt
 52 aerosol via acid displacement (Graedel and Keene, 1995, 1996; Wang et al., 2019; Erickson et al., 1999), in which
 53 the presence or uptake of other acids, such as nitric acid (HNO₃) or even organic acids (Laskin et al., 2012), shifts
 54 the equilibrium of aqueous chloride back toward gas phase HCl, as in Reaction (R2) (Brimblecombe and Clegg,
 55 1988; Clegg and Brimblecombe, 1986):



59 Additional contributions to the HCl budget come from volcanic emissions (von Glasow et al., 2009; Graedel and
 60 Keene, 1996) and anthropogenic emissions, including coal combustion, biomass burning, industrial processes
 61 (e.g., smelting, cement production), and solid waste incineration (Zhang et al., 2022; Fu et al., 2018; Keene et al.,
 62 1999; McCulloch et al., 1999; Ren et al., 2017; Wang et al., 2019). The loss processes for HCl are governed by
 63 two major sinks: reaction with hydroxyl radical and deposition. The reaction of HCl with hydroxyl radical in
 64 Reaction (R3) directly produces chlorine radicals that can participate in tropospheric oxidation, but is relatively
 65 slow ($k = 7.8 \times 10^{-13} \text{ cm}^3 \text{ molecule}^{-1} \text{ s}^{-1}$ at 298 K) (Atkinson et al., 2007):



69 While deposition of HCl removes a chlorine atom from the gas phase, its eventual uptake into an aqueous solution
 70 will produce chloride ions that can be reintroduced into the atmosphere, either by deacidification (as in R2), or
 71 via oxidation into other volatile molecular halogens (i.e., Cl₂, ICl, BrCl) (Abbatt et al., 2010; Fickert et al., 1999;
 72 Frinak and Abbatt, 2006; Knipping et al., 2000; Oum et al., 1998) or nitryl chloride (Behnke and Zetzsch, 1990;
 73 Behnke et al., 1997, 1992). Recent field observations and modelling suggest the vast majority of tropospheric
 74 HCl can be found within 1 km of the surface, with mixing ratios decreasing with height until reaching the
 75 tropopause, where mixing ratios begin increasing again (Wang et al., 2019, 2021; Lee et al., 2018; Haskins et al.,
 76 2018). In the lower troposphere, ambient HCl mixing ratios are typically observed between 10¹ and 10³ parts per
 77 trillion by volume (pptv), with the highest amounts found in polluted, coastal regions (Angelucci et al., 2021;
 78 Crisp et al., 2014, and references therein; Tao et al., 2022).

79 Recent technological advances have enabled the production of suitable instrumentation for online, in situ
80 detection of ambient HCl. Chemical ionisation mass spectrometry (CIMS) is one such method, and has been
81 previously characterized in laboratory studies by 3σ limits of detection as low as 15 pptv and sensitivities as high
82 as 2-4 counts sec^{-1} pptv $^{-1}$ (Eger et al., 2019a; Marcy et al., 2004; Roberts et al., 2010). CIMS instruments are also
83 robust enough to deploy on mobile platforms, including aircraft (Marcy et al., 2004; Veres et al., 2008) and ships
84 (Eger et al., 2019b). The primary disadvantages to CIMS exist in the possibility of sampling compounds (e.g.,
85 water) that may interfere with the desired ionisation chemistry (e.g., Marcy et al., 2004), as well as issues of
86 selectivity arising from non-analytes that create signal interferences at the desired mass-to-charge ratios meant to
87 represent HCl and/or confirm appropriate isotopic ratios and high limits of detection (Eger et al., 2019a; Roberts
88 et al., 2010). Additionally, CIMS instruments can be quite heavy, require low vacuums, have high power
89 consumption, and often require use of large amounts of consumables (e.g., N₂ gas).

90 An alternative, well-understood approach for HCl detection is infrared absorption spectroscopy. Optical
91 methods benefit from analysing well-defined and spectrally isolated HCl absorption features (Toth et al., 1970;
92 Li et al., 2011), resulting in a virtually absolute and specific measurement technique. Previously published
93 literature for laser-based HCl instrumentation has demonstrated potential efficacy for in situ detection, including
94 cavity-enhanced (Wilkerson et al., 2021; Hagen et al., 2014; Furlani et al., 2021) and multi-pass cells (Harris et
95 al., 1992; Webster et al., 1994; Scott et al., 1999), both of which benefit from path lengths spanning hundreds of
96 meters to kilometers. These instruments have also been tested on mobile platforms, such as ships (Harris et al.,
97 1992), aircraft (Webster et al., 1994), and balloons (Scott et al., 1999; Wilkerson et al., 2021). The development
98 of small, thermoelectrically cooled, interband cascade lasers (ICLs) in recent years has increased the portability
99 of these instruments while also allowing the ability to probe the major HCl infrared absorption feature wavelength
100 ($\sim 3.42 \mu\text{m}$).

101 CIMS and optical methods have both proven to be excellent means of gas phase HCl detection. However,
102 quantitative sampling remains a challenge for all existing measurement techniques. Hydrogen chloride has a large
103 dipole moment and strong hydrophilicity, which makes it susceptible to interactions with polar surface groups,
104 or surfaces on which water may be present. This “sticky” behavior results in long instrument response times
105 during HCl concentration changes (e.g., > 60 seconds) under sampling configurations that include sample tubing
106 and particle filters (Furlani et al., 2021). Further, even inert surfaces, such as those made from
107 polytetrafluoroethylene (PTFE) or perfluoroalkoxy (PFA) Teflon, contain sites where HCl or other sticky
108 molecules (e.g., HNO₃) may sorb (Roscioli et al., 2016; Neuman et al., 1999; Yokelson et al., 2003); it ~~is~~ has also
109 been estimated that PFA Teflon tubing may contain water films between 0.1-10 μm thickness at 20-50% relative
110 humidity, which will readily interact with small polar molecules (Liu et al., 2019; Laasonen and Klein, 1997).
111 Several coatings have been reported in the literature to improve sticky-compound transmission, including
112 halocarbon wax applied to glass (Yokelson et al., 2003; Webster et al., 1994), inert silicon coatings applied to
113 stainless steel (Wilkerson et al., 2021), and continual flow of polyfluorinated acid vapor across glass and Teflon
114 (Roscioli et al., 2016).

115 In this work, we present an **novel** optical method for the **detection** **quantification** of HCl: Tunable Laser
116 Infrared Direct Absorption Spectroscopy (TILDAS), combined with a sampling methodology to minimise inlet
117 artefacts. The TILDAS technique has the advantage of being highly sensitive due to its 204 m pathlength, a fast
118 response time via incorporation of “active passivation,” and being virtually specific for HCl.

119 **2 Materials and experimental methods**120 **2.1 Gases and Chemicals**

121 For in-lab experiments, dry air for sample background measurements was generated with an air compressor and
 122 dehumidifying system (dew point approximately -60° C, absolute water vapor concentration ~0.01%). When
 123 testing the effects of water on the sampling configuration in the laboratory, air was manually humidified using a
 124 Michell Instruments DG-3 Dewpoint Generator. This compressed air system was also used in generating nitrogen
 125 (N_2) gas with a commercial N_2 generator (Infinity NM32L, Peak Scientific Instruments, United Kingdom), which
 126 was used as carrier gas for active passivation (Sect. 2.3) and permeation sources (Sect. 2.4). During field studies,
 127 zero-grade air (270028-L, BOC Limited, United Kingdom) and oxygen-free N_2 (44-W, BOC Limited, United
 128 Kingdom) were used for these purposes (Sect. 2.5).

129 Perfluorobutanesulfonic acid (PFBS, 97% purity, CAS 375-73-5, Sigma Aldrich, United States) was used
 130 to actively chemically passivate inlet surfaces (Sect. 2.3). Concentrated HCl solution (37% HCl, CAS 7647-01-
 131 0, Fisher Scientific, United States) and concentrated nitric acid (HNO_3) solution (70%, CAS 7697-37-2, Fisher
 132 Scientific, United States) were used in making permeation source standards (Sect. 2.4). A 5 ppm HCl gas cylinder
 133 (diluted in N_2 , certified as 4.7 ppm \pm 5%, 2760716, BOC Limited, United Kingdom) was used as an independent
 134 method validation standard (Sect. 2.4).

135 **2.2 HCl-TILDAS**136 **2.2.1 TILDAS Design**

137 The HCl-TILDAS instrument was developed at and purchased from Aerodyne Research Inc (ARI) (McManus et
 138 al., 2011, 2015). The TILDAS design used herein has been described extensively by McManus et al. (2015,
 139 2011), and we refer the reader to these publications for technical details on the instrument schematic, physical
 140 basis of operation, and instrument noise analysis. The underlying principle of the ~~tunable infrared laser direct~~
 141 ~~absorption spectrometry~~ (TILDAS) technique is infrared absorption spectroscopy. Briefly, light from a 3 μ m-
 142 interband cascade laser (operated at 24.03°C) is collected by an objective, and then is focused through a flip-in
 143 pinhole, removed during sampling. After this focus, the beam is reimaged into the multi-pass, astigmatic Herriott
 144 cell. In addition, a beam splitter enables the laser to travel down a reference path used intermittently to measure
 145 and verify the laser tuning rate. The Herriott cell used in this instrument has an effective path length of 204 m,
 146 and is held to a temperature of 29 °C by circulating air past temperature controlled liquid along the sides of the
 147 instrument (Oasis Model T-Three). Temperature controlling the interior of the TILDAS mitigates the effects of
 148 exterior temperature changes that may cause optical fringe effects in the reported mixing ratios or changes to the
 149 mirror and table distances that may affect the path travelled by the laser light reaching the detector.

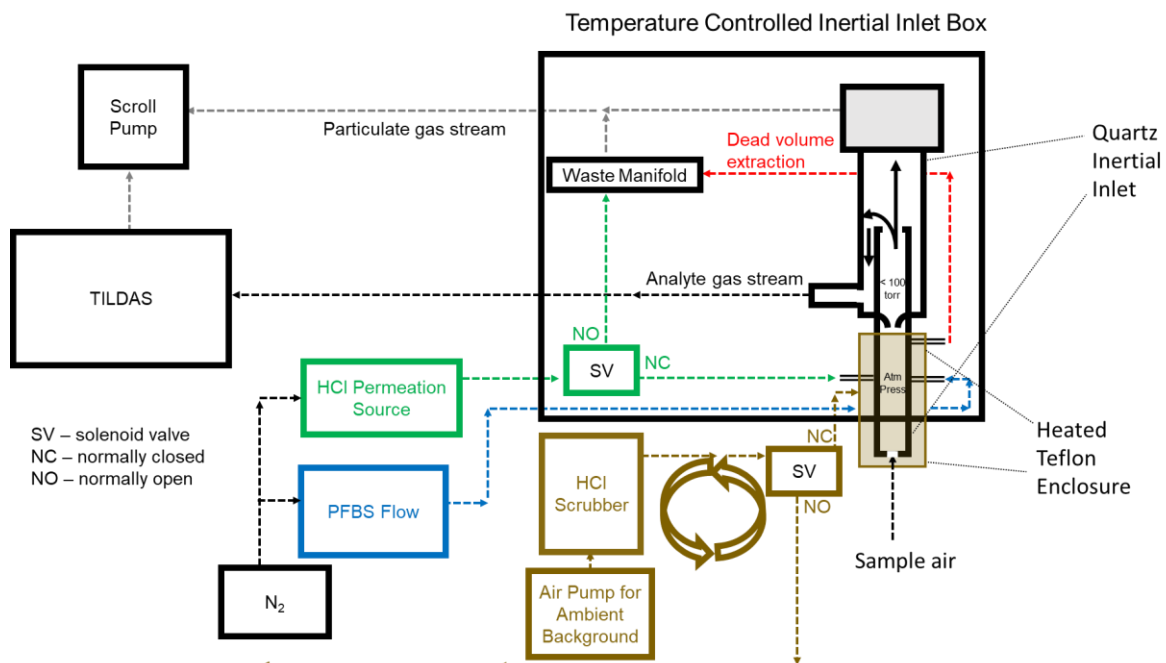
150 The instrument software sweeps the laser over the desired spectral window (2925.80 to 2926.75 cm^{-1}),
 151 which it can find via strong absorption lines from other spectrally close absorbers, including methane (2926.18
 152 cm^{-1} , 2926.700231 cm^{-1}) and water (2926.456 cm^{-1} , 2926.742 cm^{-1}) (see Fig. A1 for a HITRAN simulation of the
 153 transmittance spectrum). These lines are used to fix peak locations via a frequency-locking algorithm in the
 154 software. This Incident laser radiation (inherent laser linewidth $<0.001\text{ cm}^{-1}$), probes the strong R(1) $H^{35}Cl$ line
 155 (2925.89645 cm^{-1}) of the (1-0) rovibrational absorption band near 3.4 μ m (Guelachvili et al., 1981); the line
 156 positions for HCl are extremely well known ($\pm 0.0002\text{ cm}^{-1}$), with a corresponding line strength of 4.198×10^{-19}

157 cm/molecule (uncertainties ranging between 1-2%) (Li et al., 2013). In addition, the laser is coincidentally able
158 to estimate concentrations of methanol (2925.851 cm⁻¹, 2925.998 cm⁻¹), formaldehyde (2925.842 cm⁻¹, 2926.1
159 cm⁻¹), and nitrogen dioxide (2925.8 cm⁻¹, 2926.128 cm⁻¹). Line strengths for all species are based upon the
160 HITRAN 2016 database (Gordon et al., 2017). Spectral fits are non-linear least squares fits of a ~1 cm⁻¹ spectral
161 window, using a nonlinear least-squares fit that includes a polynomial baseline. Pressure and temperature are
162 included in the fit to account for pressure broadening and rovibrational state populations, respectively. Since the
163 absorbing features in this region are well-resolved (FWHM = 0.010 cm⁻¹, which is primarily pressure- and
164 doppler-broadened) and included on the spectral fit, spectral interferences for HCl are not expected for typical
165 ambient mixing ratios observed for the above species.

166 **2.2.2 Sampling Inlet**

167 Filtration of particulate matter is required to protect and maintain the efficacy of the multi-pass optics
168 described in the previous section (McManus et al., 1995), as well as reduce the potential of scattering and
169 absorption from particulates within the cell. However, traditional paper filters and filter holders provide surfaces
170 onto which HCl may be removed from the sample stream, both lowering the observed concentration and providing
171 a reservoir of HCl that could be later forced back into the gas phase via an acid displacement mechanism analogous
172 to that which occurs on particulates (i.e., Reaction R2) (Roscioli et al., 2016; Beichert and Finlayson-Pitts, 1996).
173 To obviate this problem, a custom-fabricated quartz virtual impactor (hereafter referred to as “inertial inlet”) was
174 added into the instrument sampling line (Fig. 1). The inertial inlet glass is housed within a temperature-controlled
175 enclosure set to 50 °C (Omega CNi32). Sample air that enters the inertial inlet is accelerated ~~passes from an~~
176 ~~ambient pressure region~~ through a critical orifice into a low-pressure region (< 100 torr). The resulting flow rate
177 through the instrument was determined by the size of ~~the~~ this critical orifice in the inertial inlet and cell pressure
178 (set to approximately 40 torr); because different inlets were used for these experiments, ~~experimental~~ flow rates
179 were 2.8, 3.7 or 12.7 L min⁻¹, yielding cell residence times (1/e) of 2.0 s and 1.5 s, and 0.4 s respectively. Once
180 in the low-pressure region, particulate separation occurs as follows: large particles (>300 nm diameter) have large
181 forward momentum and ~~travel straight~~ maintain their forward flow into a waste flow path (approximately 13% of
182 the total volumetric flow; ~~flow restriction was dictated by a separate critical orifice installed in the waste-flow~~
183 ~~path~~). Meanwhile, gas molecules and particles with an approximate diameter < 300 nm have less inertia and can
184 make the 180° turn necessary to continue along the sample flow path into the TILDAS (approximately 87% of the
185 total volumetric flow); because the astigmatic Herriott cell used in the TILDAS has a shorter path length / higher
186 light throughput than high finesse cavity systems, it is not as sensitive to decreased light throughput caused by the
187 accumulation of smaller diameter particulate matter on cell mirrors. Air flow paths can be visualized in Fig. 1.
188 The inertial inlet is connected to the HCl-TILDAS via 3m of insulated, temperature controlled (50 °C), 3/8” PFA
189 Teflon tubing.

190

191 **Figure 1: Experimental flow schematic for sampling HCl**192 **2.3 Active Passivation**

193 It has been previously shown that adding a small, continuous flow of PFBS vapor to sampling lines is effective at
 194 increasing transmission of HNO₃ through sampling tubing (Roscioli et al., 2016). This technique was used in this
 195 work to minimize loss of HCl to surfaces between the inertial inlet and the optical cell. Approximately 5-mL of
 196 PFBS was ~~contained within~~ decanted into a bubbler (made from perfluoroalkoxy (PFA) Teflon or Pyrex for
 197 laboratory and field studies, respectively) ~~within a chemical fume hood in a laboratory~~; given the growing
 198 evidence on the deleterious effects of perfluorinated compound accumulation in the environment (e.g., Buck et
 199 al., 2011), this bubbler was installed inside a sealed, IP66-rated container to insulate it from potential
 200 environmental contamination, as well as to contain any potential spillage in the event of an accident. Compressed
 201 N₂ gas was passed into the bubbler to flush the headspace (containing PFBS vapor) into the analyte flow path, just
 202 after the point of sample air entry into the inertial inlet (Fig. 1). Addition of fresh PFBS vapor into the flow path
 203 may quickly release several ppbv of HCl from unpassivated surfaces and may take several hours to ~~finish~~
 204 ~~conditioning~~ fully condition the system. The temperature and carrier gas flow rate (containing PFBS) were
 205 adjusted (between 18-22 °C and 50-100 mL min⁻¹, respectively) until no additional HCl was released to ensure
 206 optimal passivation conditions. ~~Given the growing evidence on the deleterious effects of perfluorinated compound~~
 207 ~~accumulation in the environment (e.g., Buck et al., 2011)~~, Release of PFBS vapor from the outlet of the instrument
 208 was mitigated by adding a scrubber containing hydroxide salts, glass wool, and activated charcoal to the pump
 209 exhaust. When replacement was necessary, the bubbler and any contaminated tubing were washed with absolute
 210 ethanol and fully dried before re-use, with rinsings collected and disposed of as hazardous waste.

211 Passivation efficacy was regularly tested as a function of the timescale of signal change resulting from
 212 the addition / removal of HCl standard flow into the inertial inlet (Fig. 1). Timescales were calculated as detailed
 213 in Sect. 2.6.2.

214 **2.4 HCl Standards for Technique Validation**

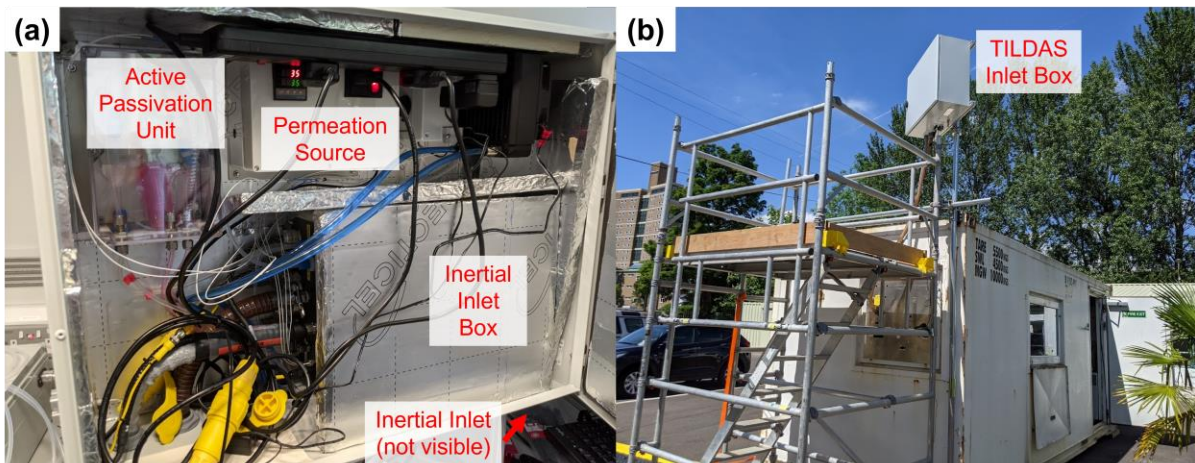
215 Custom HCl permeation sources were created for regular inlet transmission testing using a method modified from
216 Furlani et al. (2021). HCl was pipetted into a 2" length of PTFE tubing (0.118" ID, 0.157" OD, VWR). Tubing
217 was sealed by heating the ends, one at a time, in a small flame until the tubing became transparent. The end of
218 the tubing was then clamped by pliers and removed from the flame, creating a seal on cooling. The completed
219 permeation source was then placed in a temperature-controlled aluminum block (set to 35 °C). A flow (30 mL
220 min⁻¹) of N₂ gas, carries the HCl vapor into the instrument flow path (Fig. 1). Additionally, a permeation source
221 for HNO₃ was created and utilized in the same manner for the purposes of studying interferences (Sect. 3.3.2).

222 A cylinder of 5 ppmv (4.7 ± 5%) HCl (Sect. 2.1) was used to ~~confirm validate both~~ the TILDAS response
223 to HCl, ~~as well as the permeation source output~~ although the potential for losses between the cylinder and sample
224 ~~inlet mean that this was not deemed a reliable method for calibration~~. On opening the cylinder for the first time
225 (or after a period of disuse), multiple days of constant flow (controlled between 1-50 mL min⁻¹ by an Alicat MCS-
226 50SCCM) were required to condition the regulator before HCl-TILDAS reflected a stable output. Because
227 TILDAS is an optical method that relies on characteristic, well-described absorption features of molecules, it is
228 considered an absolute detection method and does not require frequent calibrations.

229 **2.5 Field Testing**

230 To demonstrate its performance as an in situ, field-ready instrument, the HCl-TILDAS was deployed during the
231 Integrated Research Observation System for Clean Air (OSCA) campaign at the University of Manchester
232 (Manchester, United Kingdom, approximately 53.444 °N, 2.216 °W), and sampled HCl between 10 June - 22 July,
233 2021. The OSCA campaign seeks to understand and assess urban air pollution and air quality at various sites
234 across the UK in order to inform and support policy makers in making future decisions, as well as evaluating the
235 impacts of decisions previously made. More information on the campaign and links to relevant studies can be
236 found here: <https://gtr.ukri.org/projects?ref=NE%2FT001917%2F1#/tabOverview>. The measurement site was
237 located at the Manchester Air Quality Super Site on the Firs Environmental Research Station at the University of
238 Manchester campus, and sampled air masses are believed to be heavily influenced by the surrounding urban
239 environment.

240 The TILDAS instrument and pump for generating background measurements (KNF Model
241 N035.1.2AN.18) were installed within an air-conditioned shipping container, held at 25 °C. The inertial inlet,
242 HCl permeation source, and active passivation unit were integrated into a separate box (80 cm x 60 cm), installed
243 above the container roof (~ 3m AGL) (Fig. 2). Because each of these components are operated at different
244 temperatures (inertial inlet box, permeation source, and active passivant held at 50, 35, and 18 °C, respectively),
245 the larger box was cooled with a water-cooling fan (controlled to 25 °C) to buffer the box interior from changes
246 in the external ambient temperatures and direct solar heating. Temperatures were regularly checked using
247 thermocouples interfaced with an Arduino Uno (Arduino).



248

249 **Figure 2: a) Field configuration for HCl TILDAS inlet system. b) Mounted inlet system at Manchester field site.**

250 During the campaign, blank measurements were obtained for 2 min out of every 10 min throughout
 251 ambient sampling periods in order to check for drifts in instrument background signal due to optical stability. An
 252 effective blank was achieved by passing ambient air through a trap composed of activated charcoal and glass
 253 wool. This HCl-scrubbed air was then directed to a Teflon encasing around the inertial inlet, which then
 254 overflowed the inlet at approximately 35 L min^{-1} , such that the inlet would only be sampling scrubbed air. To
 255 evaluate the inlet for losses and the efficacy of the PFBS, flow from the HCl permeation source was added directly
 256 into the inertial inlet on top of the background air overflow for 9 min every 3 hr. Note that overblows using zero
 257 air cylinders were found to cause a large increase in HCl signal, followed by a slow decay; it is believed this is
 258 due to the sudden disruption in the equilibrium of water molecules adsorbed to instrumentation surfaces. For this
 259 reason, permeation source additions under dry air conditions were performed overnight when ambient HCl
 260 chemistry mixing ratios were believed to be low. For these experiments, compressed dry air (produced by Jun
 261 Air OF302-25MQ2) overflowed the inlet for 1 hr, and permeation source HCl was added across three 10-min
 262 intervals within this hour.

263 **2.6 Data Analysis**

264 Data processing for this work, including background corrections and uncertainty analysis, were conducted
 265 primarily using the *R* statistical software (R Core Team, 2021) in tandem with the RStudio environment (RStudio
 266 Team, 2021).

267 **2.6.1 Background Correction**

268 As discussed above, background measurements were obtained for 2 min out of every 10 min sampling period.
 269 The median of the final 30s of each background period was used as an offset value. Offset values between these
 270 points were estimated by linear interpolation and were subsequently subtracted from ambient observations for
 271 analysis.

272 **2.6.2 HCl Signal Response Timescales**

273 Timescales of signal decay (τ) after removal of a HCl standard (Sect. 2.4) from the HCl-TILDAS sampling line
 274 were calculated as an objective measure of the sampling method performance. Such timescales for sticky gases

275 (including HCl) have been previously determined by fitting data to a biexponential model (Roscioli et al., 2016;
 276 Zahniser et al., 1995; Ellis et al., 2010; Pollack et al., 2019):

$$277 \quad y = A_1 \exp\left(-\frac{t}{\tau_1}\right) + A_2 \exp\left(-\frac{t}{\tau_2}\right) \quad (1)$$

278 where y represents the HCl mixing ratio, t represents elapsed time, both A_1 and A_2 are proportionality terms, and
 279 both τ_1 and τ_2 control the shape of the decay curve. Herein, both single exponential and biexponential models
 280 were fit to the data to determine the time needed to reach $1/e$ (τ), 75% (τ_{75}), and 90% (τ_{90}) of a starting HCl
 281 concentration. The fitting function within R (i.e., “nls”) required initial guesses for the A and τ terms, which were
 282 based on the starting mixing ratio of HCl and anticipated residence time of air in the absorption cell, respectively;
 283 however, the function was not constrained to these values in formulating its output.

284 **2.6.3 HCl Partitioning**

285 The thermodynamic equilibrium model ISORROPIA II (Fountoukis and Nenes, 2007), used to investigate K^+ –
 286 Ca^{2+} – Mg^{2+} – NH_4^+ – Na^+ – SO_4^{2-} – NO_3^- – Cl^- – H_2O aerosol systems, was employed to estimate the potential that
 287 particulate chloride (pCl^-) may partition to HCl within the heated inlet system. Calculations were performed in
 288 ‘forward mode’ when possible, in which the total (gas + aerosol) concentrations of NH_3 , H_2SO_4 , HCl, HNO_3 , Na^+ ,
 289 Ca^{2+} , K^+ , and Mg^{2+} were specified, alongside ambient temperatures and relative humidities. The model then solves
 290 a series of equilibrium equations based on these conditions, incorporating water activity equations, activity
 291 coefficient calculations, electroneutrality, and mass conservation, to determine the gas and aerosol concentrations
 292 at thermodynamic equilibrium. The calculations were then repeated for different potential TILDAS sample line
 293 testing temperatures (35, 50 and 80°C) to determine changes in gaseous HCl mixing ratios resulting from re-
 294 partition with aerosols within the sample line. In scenarios where gas phase concentrations were unknown, the
 295 model was initialised in ‘reverse mode’ with averaged aerosol concentrations to predict gas phase concentrations
 296 at equilibrium. In all model calculations, the aerosol was assumed to be in a thermodynamically stable state, in
 297 which salts precipitate if saturation is exceeded, owing to the low relative humidities within the heated inlet line.

298 **3 Results & Discussion**

299 **3.1 Instrument Performance**

300 The performance metrics of HCl-TILDAS are compared with previously described optical methods in Table 1.
 301 Allan-Werle deviations were calculated in the laboratory while overflowing the inlet with dry zero air (Sect 2.5)
 302 (Hagen et al., 2014; Furlani et al., 2021), and in the field with HCl-scrubbed sample air (i.e., without removal of
 303 water vapor) (Fig. 3). Under 30s integration times and using the 3.7 L min⁻¹ inlet, the precision (1-2 pptv at 1 σ)
 304 and 3 σ limit of detection (4-6 pptv) outperform previously reported methods, which range from 6 - 100 pptv
 305 precision, and 18 - 78 pptv limits of detection under 30 s averaging times. HCl-TILDAS has clear advantages for
 306 both figures of merit if longer integration times are considered; for dry, laboratory conditions, we achieved a
 307 precision of 0.5 pptv and corresponding LOD of 1.6 pptv at the Allan minimum of 2.4 minutes, compared with
 308 1.5 pptv precision and 4.4 pptv LOD for field observations at an Allan minimum of 56 seconds. These values are
 309 more than adequate for obtaining high quality field observations at the expected ambient HCl mixing ratios of
 310 10^1 - 10^3 pptv (Wang et al., 2019). [The better performance of the HCl TILDAS is achieved using a long pathlength](#)

311 (200 m), measuring absorptions in the mid-infrared by probing the fundamental ro-vibrational absorption band
 312 (which has much larger cross-section than in the near-IR), and reducing light and dark noise levels to $<5 \times 10^{-6}$
 313 equivalent absorbance in 1-second.

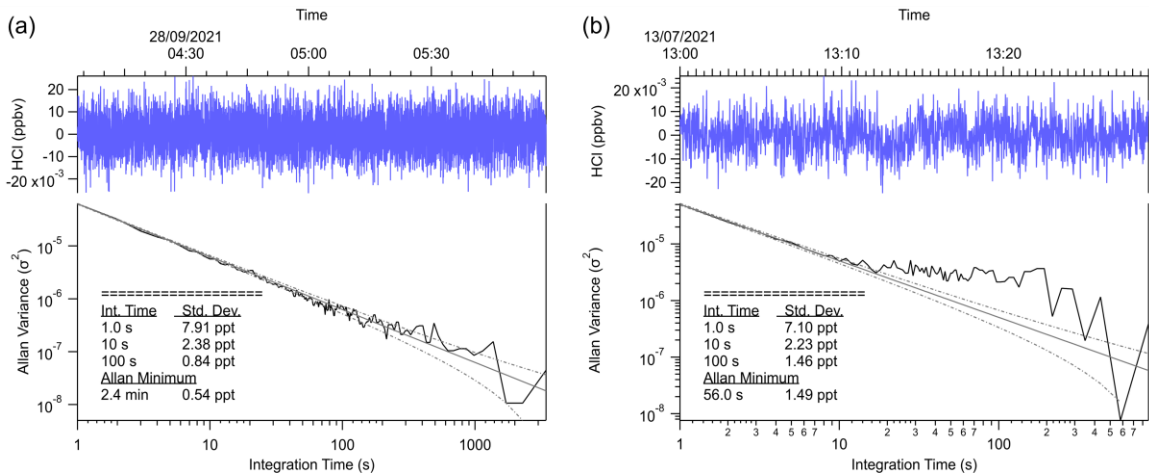
314

315 **Table 1: Summary table comparing the performance of HCl TILDAS to similar, previously reported optical methods.**

316 ^aThe lower limit of the figures of merit represent laboratory sampling, while the higher limit represents field sampling.
 317 τ_{90} are reported for dry, laboratory sampling conditions. The lower value represents laboratory analysis, while the
 318 higher value represents data from field work (Fig. 9). ^bReported for mixing ratio changes $>10^9$ per volume or higher".

Instrument	LOD	Precision	τ_{90}	Reference
HCl-TILDAS ^a	21-24 pptv (1 s) 4-6 pptv (30 s)	7-8 pptv (1 s) 1-2 pptv (30 s)	$>4.4 (\pm 0.3)$ s (2.8 L min ⁻¹) $>1.15 (\pm 0.06)$ s (12.7 L min ⁻¹)	This study
Near-IR CRDS	< 18 pptv (30 s)	6 pptv (30 s)	> 10 s	Furlani et al. (2021)
Near-IR CRDS	60 pptv (60 s)	20 pptv (60 s)	10 - 15 s	Hagen et al. (2014)
Off-axis integrated cavity output spectrometer (OA-ICOS)	78 pptv (30 s)	26 pptv (30 s)	10 s	Wilkerson et al. (2021)
Aircraft laser infrared absorption spectrometer (ALIAS)	33 pptv (30 s)	100 pptv (30 s)	10 s ^b	Webster et al. (1994)

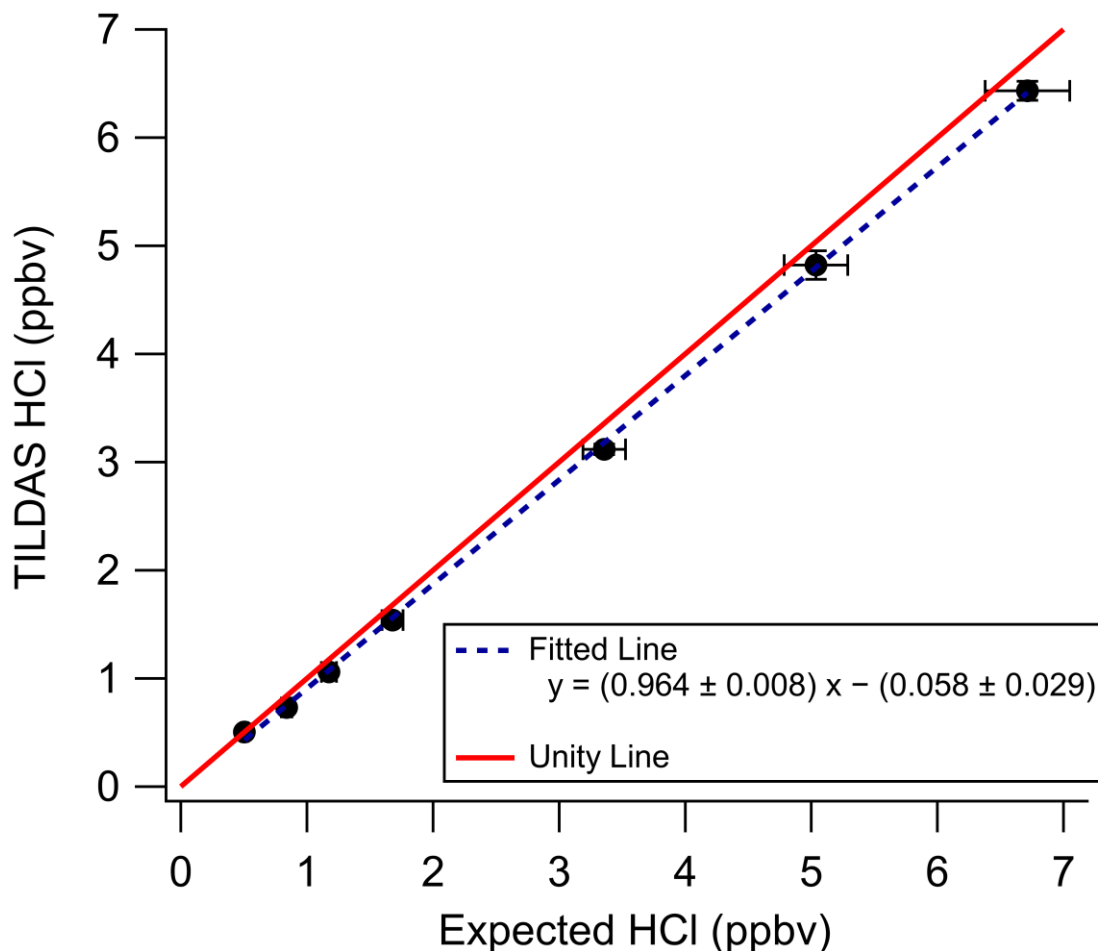
319



320 **Figure 3: Allan variance plot demonstrating the signal variance and limit of detection calculations for varying**
 321 **introduction times.**

322 A commercial HCl cylinder with a certified concentration (4.7 ppm \pm 5%) was used as an objective
 323 standard for in-lab validation. Mixing ratios were varied by adjusting the flow rate of the cylinder output, which
 324 was then directly injected into an inertial inlet sidearm (Fig. 1) for direct injection into the passivated inertial inlet.
 325 Standard HCl was then diluted into the dry, HCl-free compressed air being sampled by TILDAS. The slope
 326 obtained (0.964) was found to lie within the expected 5% uncertainty reported by the manufacturer, reflecting

327 high accuracy for TILDAS observations (Fig. 4). However, additional sources of error causing deviation from
 328 unity must be considered. For example, multiple days of HCl cylinder flow are required for the output mixing
 329 ratio to stabilize at its maximum concentration (as observed by TILDAS) after opening the cylinder; this behavior
 330 is presumably caused by uptake of HCl onto the metal cylinder regulator and Teflon tubing lines until they are
 331 fully conditioned, causing the observed signal to register lower than expected. Changes to HCl cylinder flow
 332 additionally require similar conditioning time to re-establish signal stability, likely caused by changes to the HCl
 333 gas/surface equilibrium. Thus, although the cylinder was filled with a certified concentration, we were unable to
 334 independently confirm that this matched what was ultimately delivered to the TILDAS, with an observed
 335 concentration lower than the certified being most likely due to loss onto surfaces. We therefore use this
 336 comparison as a validation of this method, and not a calibration, using the spectroscopy described above.



337

338 **Figure 4: In-lab validation of HCl-TILDAS by a commercial HCl standard. Principal axis error bars represent the**
 339 **5% uncertainty associated with the HCl standard (as reported by the manufacturer), while the vertical axis error bars**
 340 **represent 1 standard deviation of HCl-TILDAS observations for each validation point. Note the regression line here is**
 341 **used only the purpose of technique validation and is not used for calibrating data.**

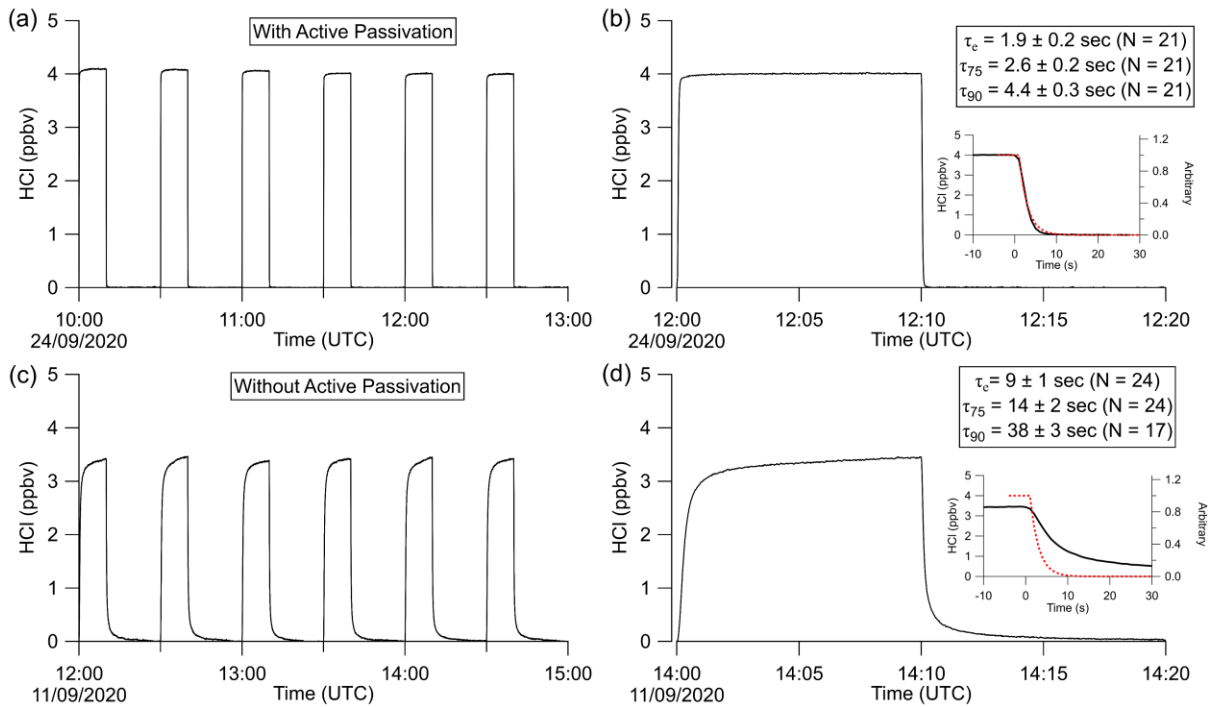
342 3.2 Evaluation of Sampling Method

343 Multiple variables were found to affect HCl transmission through the instrument flow path (Fig. 1), including the
 344 presence or absence of active passivation (i.e., whether PFBS is flowing through the sample line; Sect 3.2.1) and
 345 the presence of water vapor (Sect 3.2.2). The timescales of signal change after removal of an HCl source were

346 used to objectively compare the relative effects of each variable. They further allow for direct comparison of the
347 performance of this HCl sampling method with those previously published (Table 1). Note that these timescales
348 reflect how quickly HCl mixing ratios change within the 1.8L measurement cell and do not include the time
349 required for the sample gas to reach the cell (i.e., time zero is when a change in signal is first observed, not from
350 when an addition valve was triggered).

351 **3.2.1 Active Passivation**

352 To test the effectiveness of active passivation, HCl permeation source flow was added into the TILDAS sample
353 line for 10 min of subsequent 30 min periods using the inertial inlet with the lowest flow rate (2.8 L min^{-1}), as the
354 effects of HCl-wall interactions would be the most exaggerated. Experiments were repeated both with and without
355 the coinciding flow of PFBS (Fig. 5), and the TILDAS inlet was overflowed with dry, compressed air (Sect. 2.1),
356 such that a baseline signal was observed in the absence of permeation source addition. **We note the permeation**
357 **source concentration for these experiments was $4.1 \pm 0.3 \text{ ppbv}$; the average standard deviation during the last five**
358 **minutes of permeation source additions was calculated to be $8 \pm 2 \text{ pptv}$, while the average standard deviation of**
359 **the last five minutes of background periods was calculated as $7 \pm 1 \text{ pptv}$, demonstrating nearly identical precisions**
360 **while sampling blanks or fixed HCl concentrations.** As seen in Fig. 5a, employing active passivation yields sharp,
361 square wave-like behavior on both addition and removal of the HCl permeation source flow. From the fits of a
362 single exponential model, τ_e averaged $1.9 \pm 0.2 \text{ s}$ ($N = 21$) after HCl permeation source removal (Fig. 5b, Fig.
363 A2), which compares well with the predicted absorption cell residence time ($1/e$) of 2.0 s. Though a biexponential
364 model was also fit to these data (and achieved comparable τ_e , τ_{75} , and τ_{90} values, Table A1), the convergence
365 tolerance of the non-linear least squares solving algorithm (Sect. 2.6.2) had to be loosened by six orders of
366 magnitude (from a default value of 1×10^{-5} to 2×10^1) to achieve convergence, suggesting these results are not
367 meaningful. Indeed, the errors for the predicted variables often greatly exceeded the magnitude of the associated
368 variables themselves, suggesting a biexponential model is not appropriate for these actively passivated data.

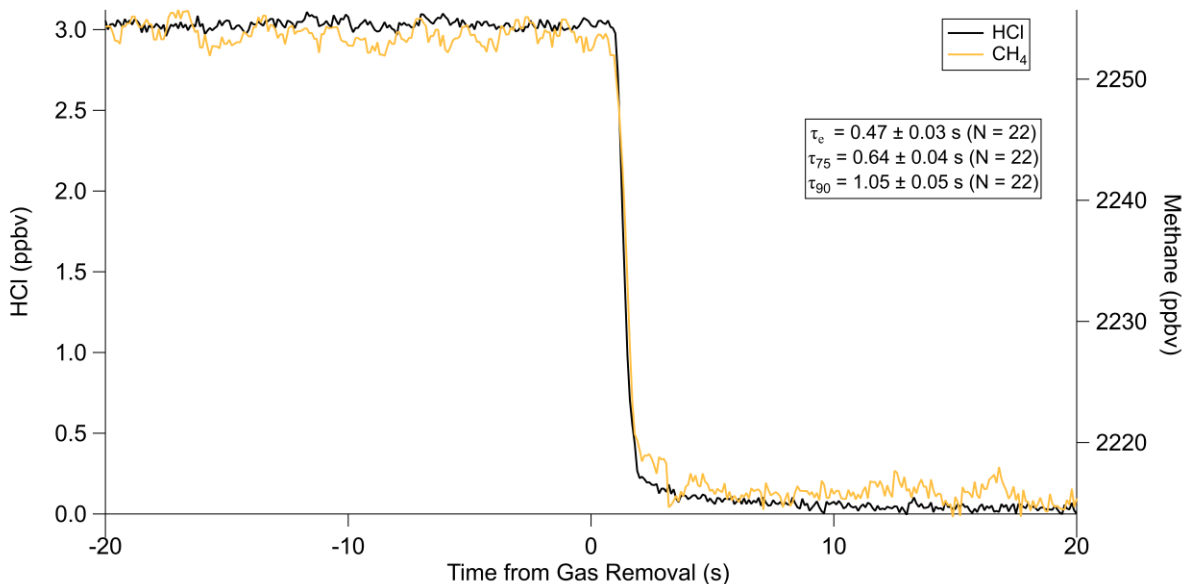


369

370 **Figure 5: Excerpted time series of HCl permeation source additions with (a, b) and without (c, d) use of active**
 371 **passivation. a) TILDAS response to HCl permeation source addition to the sample line for 10 minutes every 30 minutes.**
 372 **b) Example case from plot (a) demonstrating the profile of the decay timescales. Reported τ 's represents the mean and**
 373 **standard deviation of the entirety of these experiments. Inset shows a close-up of the actual decay compared with the**
 374 **red dashed line, representing the theoretical decay profile of a non-sticky compound modelled on the residence time of**
 375 **air in the absorption cell. Frames c) and d) are analogous to a) and b), but without use of active passivation.**

376 Without active passivation, the signal profiles of the HCl additions have comparatively slower rises, and
 377 do not reach the average HCl maximum mixing ratios of 4.03 ± 0.06 ppbv within 10 min intervals (Fig. 5a, b, Fig.
 378 A3). In these cases, biexponential models were fit without having to adjust the default convergence tolerance,
 379 and the results were found to have smaller term- and residual errors when compared to the analogous single
 380 exponential model (see Table A2). τ_e for the signal decays was calculated as 9 ± 1 s ($N = 24$), or approximately
 381 4.5 times greater than the residence time through the measurement cell (Fig. 5c, d).

382 The reported timescales in this work can be further improved by increasing the flow rate of the inlet.
 383 Using the 12.7 L min^{-1} inertial inlet, τ_e averaged 0.49 ± 0.03 s ($N=21$), comparing very well to the theoretical cell
 384 residence time ($1/e$) of 0.45 s for this flow rate (Fig. 6, Fig. A4, Table A3). τ_{90} was similarly improved, averaging
 385 1.15 ± 0.06 s. The higher flow rate clearly demonstrates that wall interactions are reduced; as demonstrated by
 386 Fig. 6, the decay rate mimics that of methane, which is a non-sticky compound also measured by the HCl-TILDAS.
 387 As the current configuration includes 3 m of heated tubing between the inertial inlet and the HCl-TILDAS itself,
 388 it is likely this response could be further improved by shortening this line.



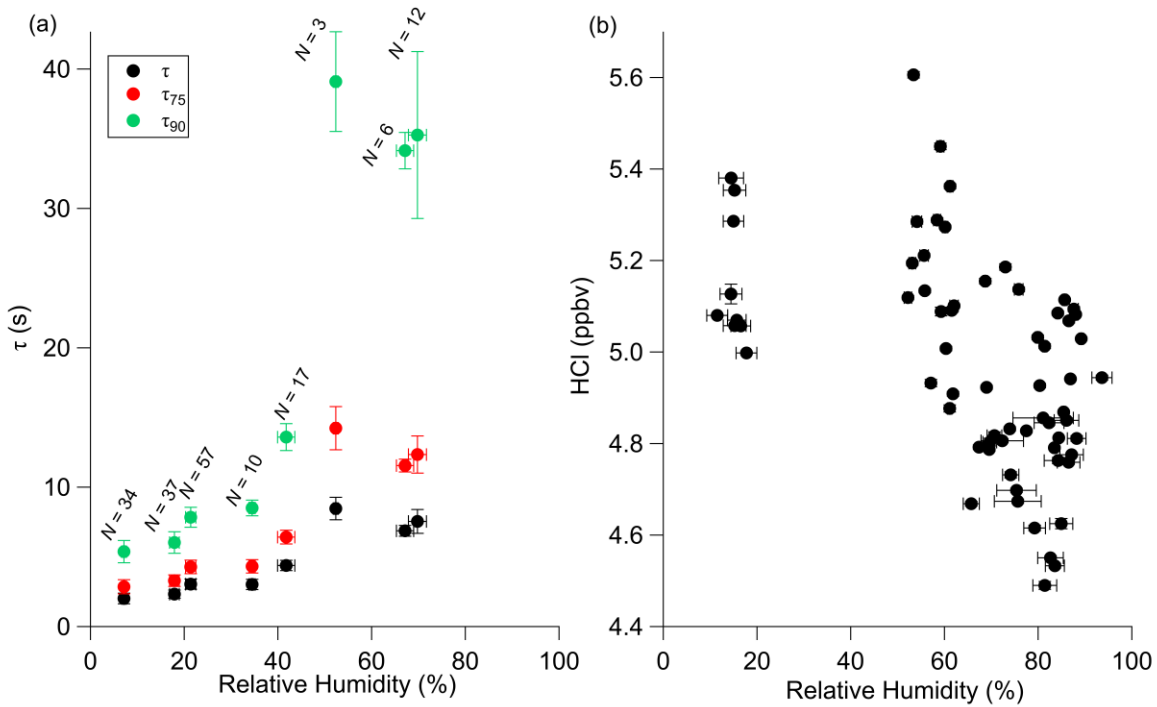
389

390 **Figure 6: Comparison of HCl decay with methane at inlet flow rate of 12.7 L min^{-1} .** Note that the methane signal
 391 represents the change in concentration from sampling a zero air cylinder (~2260 ppbv) to sampling ambient air (~2215
 392 ppbv).

393 The τ_{90} achieved utilizing active passivation in this study is the shortest reported instrument response
 394 time for changes in HCl mixing ratios to date (Table 1) and demonstrates that the use of PFBS is effective for
 395 reducing HCl-surface interactions. Previous studies have suggested that a biexponential model (Eq. 1) may better
 396 physically represent sticky gas flow through an instrument (Furlani et al., 2021; Zahniser et al., 1995; Ellis et al.,
 397 2010; Pollack et al., 2019); in this approach, τ_1 may represent the air residence time within the instrument, while
 398 τ_2 will represent the factor(s) that cause the analyte to lag through the instrument (e.g., surface interactions). Our
 399 results were not inconsistent with this postulation since the unpassivated cases were well-represented by the
 400 biexponential model (i.e., significant τ_1 and τ_2 equation terms within Eq. 1), while passivated cases were better
 401 represented by the single exponential model (i.e., dominant τ_1 but negligible τ_2). However, the results do not
 402 directly support it either; for unpassivated cases, the predicted τ_1 averaged 6.2 ± 0.7 (greater than 3 times the cell
 403 residence time for the inertial inlet used), and 69 ± 10 for τ_2 (Table A2). Further reconciliation of the physical
 404 basis behind the biexponential model is outside the scope of this work, and no attempt is made to ascribe further
 405 physical meaning to the derived coefficients.

406 3.2.2 Humidity

407 The experiments in the previous sections were conducted using dried compressed air. As dry air is not
 408 representative of ambient sampling conditions, timescale experiments were also performed with humidified
 409 sample air under passivated conditions. The results in Fig. 7a demonstrate a clear increase in τ 's with increasing
 410 relative humidity, affecting τ_{90} most prominently.



411

412 **Figure 7: Effects of changes in relative humidity on a) τ in laboratory experiments and b) HCl standard mixing ratios**
 413 **in the field. Relative humidity values are based on the TILDAS-observed water mixing ratio observed during the HCl**
 414 **decay period (a) or HCl standard addition (b), and concurrent temperature reading. Error bars for both axes represent**
 415 **one standard deviation.**

416 While Roscioli et al. (2016) note that the general effectiveness of active passivation on HNO_3 instrument
 417 response times appeared independent of humidity levels between 0-70%, the results of this experiment do not
 418 display this same behavior above approximately 40% relative humidity. Notably, the inlet flow rate used for these
 419 experiments is less than four times that used in that study (i.e., 2.8 L min^{-1} vs 14 L min^{-1}), which would increase
 420 analyte-surface interactions. However, these values do represent an improvement from the HCl sampling method
 421 reported by Furlani et al. (2021), in which τ_{90} was reported as 239s at 33% relative humidity. Similarly, [Fig. 7b](#)
 422 [demonstrates that](#) field additions of a HCl permeation source (utilizing the 3.7 L min^{-1} inertial inlet) elicited lower
 423 mixing ratios at relative humidities [greater than](#) between 60-93% (mean of $4.9 \pm 0.2 \text{ ppbv}$), contrasting with
 424 additions under dry air conditions (i.e., relative humidities $< 20\%$; mean of $5.2 \pm 0.1 \text{ ppbv}$) ([Fig. 7b](#)). This finding
 425 suggests that a permanent or semi-permanent physical loss of HCl is occurring within the sampling inlet at higher
 426 humidities, resulting in an average -5.8% bias. Both PFA tubing and silica surfaces have been previously reported
 427 to adsorb several monolayers-worth of water at room temperature in humid air (Saliba et al., 2001; Sumner et al.,
 428 2004), which would be expected to bind and solvate HCl. As both the inertial inlet and sample line were heated
 429 to 50°C , it is anticipated that this effect would be minimised by discouraging water from attaching to surfaces,
 430 but not eliminated. However, increasing the sampling temperatures may further improve both the instrument
 431 response timescale and reduce this loss effect; warmer temperatures may also increase the likelihood of HCl
 432 degassing from coarse mode particles within the inertial inlet before their removal, or from fine mode particles
 433 that may travel throughout the entire sample path (Brimblecombe and Clegg, 1988). Further discussion of the
 434 effects of particulate chloride and uncertainty estimation can be found in Sect. 3.3.1.

435 **3.3 Potential Interferences**

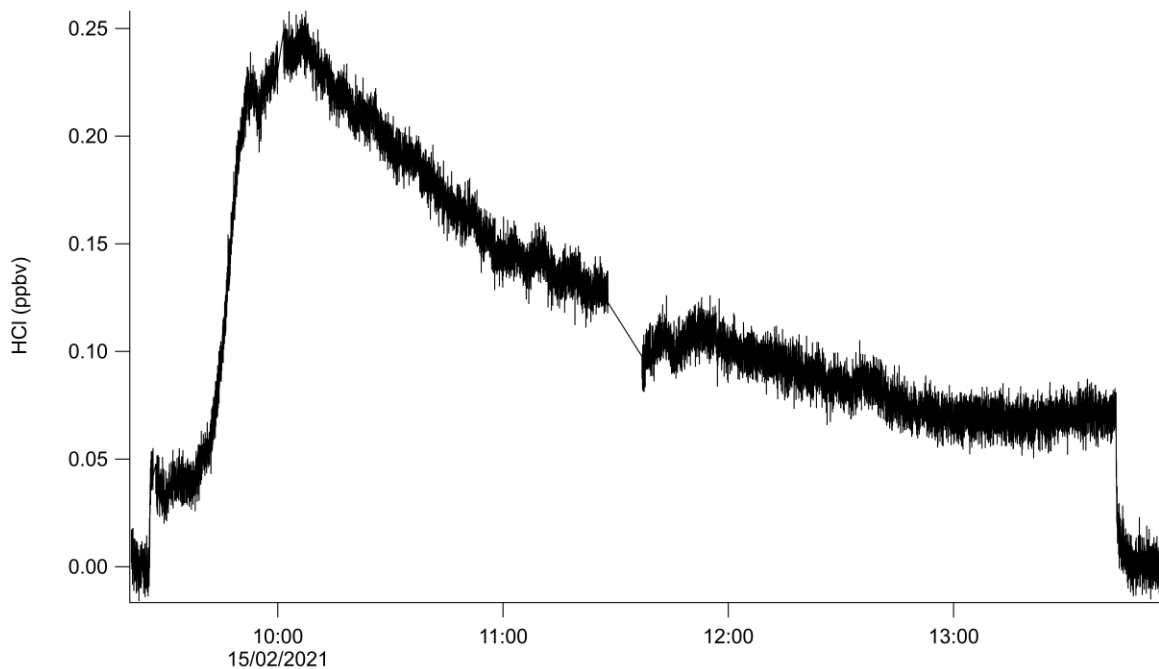
436 As discussed above, spectral interferences are not believed to play a major role in the detected HCl concentrations.
 437 However, two potential sources of undesired HCl may exist if sample gas contains a significant amount of
 438 particulate chloride (pCl^-) or other strong gaseous acids (e.g., HNO_3), discussed in more detail below.

439 **3.3.1 Effects of Particulate Chloride**

440 It is well established that HCl and particulate chloride (pCl^-) exist together in dynamic equilibrium (Fountoukis
 441 and Nenes, 2007; Clegg and Brimblecombe, 1986; Brimblecombe and Clegg, 1988; Beichert and Finlayson-Pitts,
 442 1996). The use of heated sample inlet lines (50 °C in this study) may volatilize HCl from pCl^- if sufficient heating
 443 occurs before particles are removed via impaction, yielding measurements with positive systematic error. As
 444 discussed in Sect. 2.6.3, the thermodynamic equilibrium model ISORROPIA II was used to theoretically assess
 445 the impact of pCl^- volatilisation within the heated TILDAS sample inlet on measured HCl mixing ratios based on
 446 three potential operating temperatures (35°C, 50°C, and 80°C). To simulate conditions of an inland, urban
 447 environment, averaged aerosol concentrations from London, England, were used to initiate the model (Crilley et
 448 al., 2017; Bandy et al., 2022b, a). It was estimated for the conditions of these measurements that HCl repartitioning
 449 from pCl^- would result in an increase of the HCl mixing ratio by 1 ppqv at both 35°C and 50°C, while dramatically
 450 increasing to 200 pptv at 80°C. Such increases in HCl are expected to derive from the loss of the liquid aerosol
 451 phase following the reduction in humidity experienced in the elevated temperatures of the sample inlet, and the
 452 evaporation of NH_4Cl . However, Huffman et al. (2009) reported approximately the evaporation of only 10-15%
 453 NH_4Cl aerosol through a thermodenuder held at 50 °C (12 s residence time). Based on an inertial inlet flow rate
 454 of 2.8 L min⁻¹ and a corresponding residence time of 150 ms before particulate removal via impaction, it is unlikely
 455 volatilization will significantly affect these measurements. Further in situ testing was performed during the OSCA
 456 field study, discussed further in Sect. 3.4.

457 **3.3.2 Effects of Nitric Acid**

458 The use of PFBS appears to lessen the effects of HCl surface adsorption and improve the instrument response
 459 time to changes in HCl concentrations (Fig. 5, 6). If, though, PFBS does not completely prevent HCl sorbing to
 460 walls, the sampling of acids stronger than HCl (e.g., HNO_3 , H_2SO_4) may perturb the existing passivation
 461 equilibrium on instrument surfaces. In order to test this, a HNO_3 permeation source was fabricated (Sect. 2.4) and
 462 allowed to flow into the TILDAS inlet (Fig. 8). The HNO_3 permeation source output was estimated as NO using
 463 a Mo-catalyzed NO_y convertor in tandem with a commercial NO_x analyzer (Teledyne T200). In a test experiment,
 464 the addition of 43.0 ppbv of HNO_3 to the inertial inlet caused a maximum increase of 0.29 0.25 ppbv to the HCl
 465 signal (Fig. 8). Continued addition of HNO_3 eventually causes the signal to plateau at a higher background, ~0.08
 466 ppbv above the original background. This experiment was designed as a worst-case scenario, as the TILDAS had
 467 been periodically sampling a high concentration HCl permeation source prior to the HNO_3 addition (as would be
 468 the case during field operation). This results in more HCl exposure to inlet surfaces than otherwise would be from
 469 purely ambient sampling conditions.



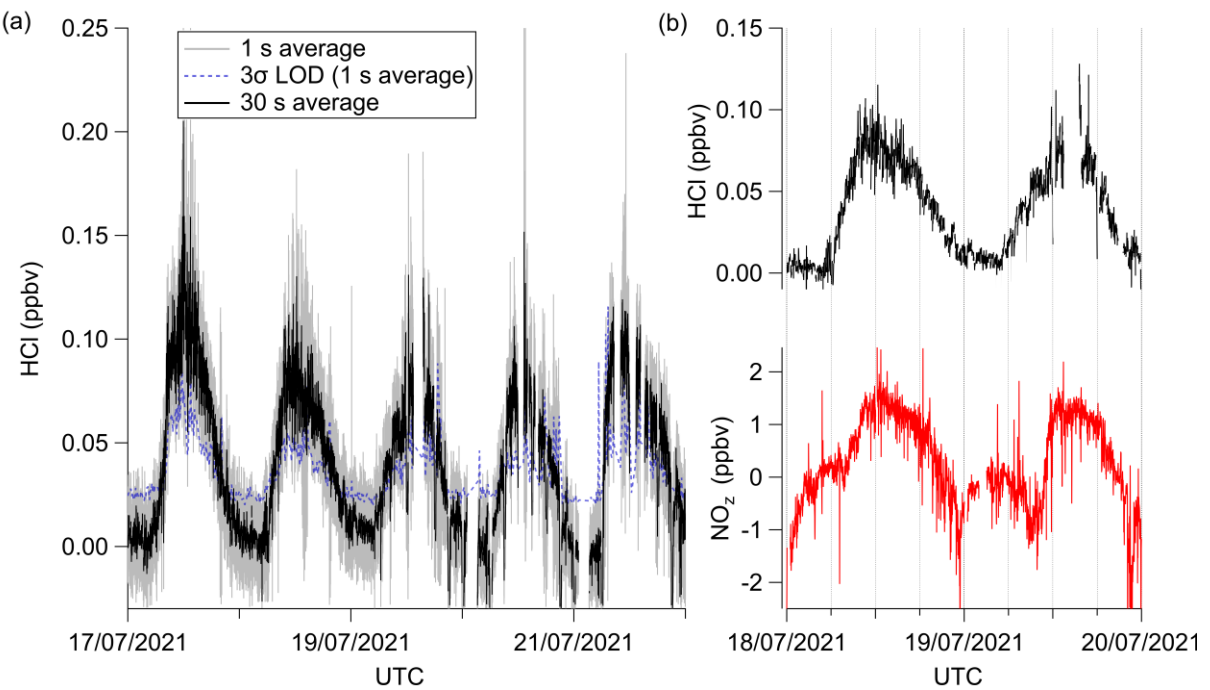
470
 471 **Figure 8: Demonstration of the effects of 43.0 ppbv nitric acid addition to the passivated sample inlet flow at**
 472 **approximately 13:00 09:45UTC.**

473 There is no absorption band overlap between HNO_3 and HCl in the analyzed spectral region, strongly
 474 indicating the observed increase in HCl signal occurred due to additional HCl molecules reaching the absorption
 475 cell. It is plausible this occurs because of interactions between HNO_3 and surfaces where HCl may be adsorbed,
 476 or with sampled particulates (although not in this specific case, due to the particle free air being used). One
 477 possible mechanism is that the HNO_3 increases competition for sorption sites, and ultimately replaces HCl on the
 478 surface. In this scenario, expected behavior would be a gradual increase in the background HCl signal as the
 479 stronger acid removes available sorption sites, and increased HCl throughput is achieved. A second mechanism
 480 would occur if water or particulate Cl^- are present on instrument surfaces; here, the diffusion of the HNO_3 into the
 481 water would cause acid displacement of HCl , as in Reaction (R2). If the strong acid flux were large enough, a
 482 sharp HCl signal increase (commensurate with the magnitude of available Cl^-) would be anticipated from HCl
 483 off-gassing that would gradually recover as a new equilibrium is established. As seen in Fig. 8, it appears that a
 484 combination of these mechanisms is present. Once equilibrium had been established with addition of HNO_3 , flow
 485 from additional HNO_3 permeation sources were added to the inertial inlet to observe whether additional HCl
 486 would be driven off (results not shown). However, each addition of HNO_3 resulted in similar spikes and signal
 487 recoveries to elevated HCl background levels. As the sudden introduction of 34.0 ppbv HNO_3 into the TILDAS
 488 inlet produced < 10% of a signal response, it is likely a more gradual introduction of HNO_3 would elicit a
 489 proportionally smaller HCl signal. Further, Fig. 8 was produced using an inertial inlet flow rate of 2.8 L min^{-1} ;
 490 these mechanisms are expected to be further reduced using faster-flow inlets (e.g., 12.7 L min^{-1}), which would
 491 both reduce gas-surface interactions, as well as make the mixing ratio transient proportionally smaller. **In any**
 492 **case, this result demonstrates the importance of reducing the ability of HCl to stick to inlet / instrument surfaces.**

493 While this interference was shown to be of potential significance in a laboratory context, in situ effects
 494 cannot be quantified without concurrent HNO_3 (or proxy) observations. To this end, **estimations** an examination
 495 of how HNO_3 affects our method in a real-world context are further explored in Sect. 3.4.

496 **3.4 Field Sampling**

497 Field observations for HCl-TILDAS were obtained during the Summer 2021 OSCA campaign, hosted at the
 498 University of Manchester (Sect. 2.4; Fig. 9). These represent the second high frequency tropospheric field
 499 measurement of HCl reported by optical techniques (Angelucci et al., 2021). For the period presented, ambient
 500 relative humidity ranged from 36-98%, and corresponded with average τ_e of 2.8 ± 0.3 s ($\tau_{90} = 7 \pm 1$ s). Because
 501 the inertial inlet used in this study had a flow rate of 3.7 L min^{-1} , the expected $1/e$ residence time in the Herriott
 502 cell is approximately 1.5 s; these longer empirical instrument response timescales indicate incomplete passivation
 503 of inlet surfaces. Further, as discussed in Sect. 3.2.2, it is expected that the magnitude of the HCl measurements
 504 will be biased low by as much as 5.8% in this campaign due to inlet surface losses, quantified through regular
 505 field additions of a HCl permeation standard (Fig. 7). **Periods where the data spiked into negative values may**
 506 **have been caused by faulty blanks, and are deemed below the instrument's 3σ limit of detection.**



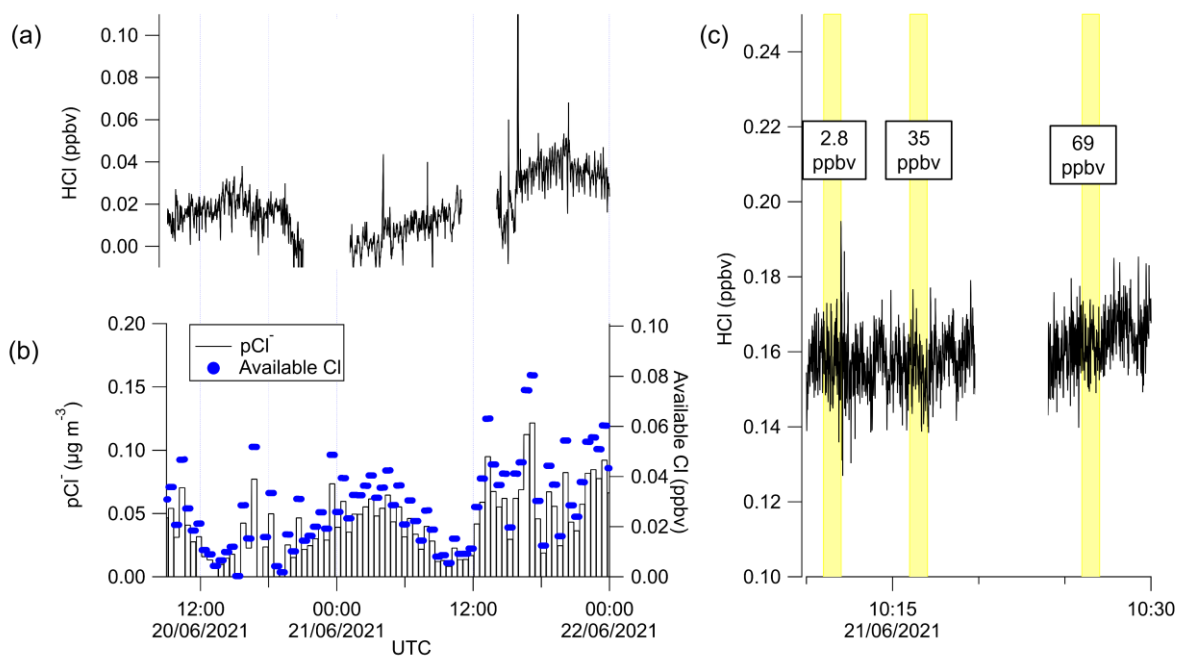
507 **Figure 9 – Excerpted field data from summer OSCA 2021 campaign.** a) Averaged time series during the final week of
 508 measurements, in which grey represents 1 s data collection frequency, dashed-blue represents the 1Hz 3σ limit of
 509 detection, and while the black trace represents 30 s averages of these same HCl data. b) Comparison of HCl time series
 510 (top) and concurrent NO_z time series, both averaged to 1 min. **Gaps in data result from additions of high concentration**
 511 **HCl standards that do not reflect ambient values. The increased noise on the data around these time periods is likely**
 512 **due to inlet effects following the HCl additions.**

514 Additional sources of uncertainty may be introduced from plumes of HNO₃ sampled by our inlet, as
 515 discussed in Sect. 3.3.2. While no direct HNO₃ measurement was obtained during the OSCA campaign, NO_z was
 516 used as an approximation, calculated from co-located NO_x and NO_y observations (NO_z = NO_y – NO – NO₂)
 517 (Watson, 2022c, b). **We note that this NO_z measurement is highly uncertain due to the method of subtraction used**
 518 **to calculate NO_z, and the potential for other sources of NO_z aside from HNO₃ (San Martini et al., 2006), and is**
 519 **therefore used only for comparative purposes.** For the period presented in Fig. 9b, a Pearson correlation coefficient
 520 (r) of 0.69 was found between HCl and NO_z. Given both compounds ambient production pathways are expected
 521 to follow a photochemically driven diurnal cycle, this suggestion of linearity is not surprising. However, the
 522 profiles themselves differ, with changes in NO_z lagging changes in HCl. For example, HCl mixing ratios begin

523 to rise at 06:00 on 18 July 2021, while NO_z mixing ratios remain comparatively plateaued until 08:00, when it
524 begins its rise. A similar pattern repeats on 19 July 2021, in which HCl mixing ratios begin rising just before
525 06:00, and NO_z mixing ratios again do not increase until 08:00. The sharp increase in NO_z mixing ratios after
526 08:00 is not followed by an in-kind increase in HCl mixing ratios; if HNO_3 were eliciting HCl within the sample
527 inlet, it would be expected fluxes of HNO_3 would precede or coincide with increases in HCl. As such, we do not
528 believe HNO_3 is a significant interference within our inlet for the period analysed here.

529 To test the extent to which pCl^- may repartition to HCl, a denuder was temporarily fitted in line to sample
530 only pCl^- ; consequently, any HCl observed during the time period could be attributed to the re-partitioning of pCl^-
531 within the TILDAS sample inlet (Fig. 10). To confirm the efficacy of removing HCl gas, cylinder additions that
532 result in TILDAS observed mixing ratios of 2.8, 35, and 69 ppbv were injected through the denuder for 60s with
533 no corresponding increase in TILDAS signal (Fig. 10c). For the period presented, HCl signal was seen to range
534 between limits of detection to peaking at 53 pptv. ISORROPIA was used to test how much HCl may originate
535 from pCl^- in the conditions during the OSCA campaign, utilizing co-located measurements of total (gas + aerosol)
536 concentrations of NH_3 (using a Los Gatos Research ammonia analyzer) and HNO_3 (as NO_z) (Watson, 2022c, b,
537 a) within the heated inlet system using the ‘forward’ mode in ISORROPIA (no metals were included in these
538 calculations). Based on these simulations, it was expected that the majority of pCl^- would partition into the gas
539 phase upon reaching thermal equilibrium in the sample inlet leading to systematic errors of up to 40, 43, and 48
540 pptv at 308, 323, and 353 K respectively. While the HCl signal did reach these values while the denuder was
541 installed, no direct relationship was observed between the HCl signal and concurrent pCl^- measurements (Fig.
542 10a, b). In particular, there are instances (e.g., between 12:00-15:00 on 21 June 2022²¹) where the available
543 chlorine (calculated as the mixing ratio of chlorine if it were entirely released from particulates) is less than HCl
544 observations. This may suggest a potential leak between the denuder and the inertial inlet that could allow a small
545 volume of ambient air to contaminate the air sample, obfuscating accurate interpretation of these results. While
546 a strong relationship was not observed between the pCl^- and HCl signals (with denuder) in the period observed
547 here, the ISORROPIA predictions emphasize that this is a significant possible source of positive error in HCl
548 measurements whenever heated sample lines are used for HCl sampling in the presence of particulates.

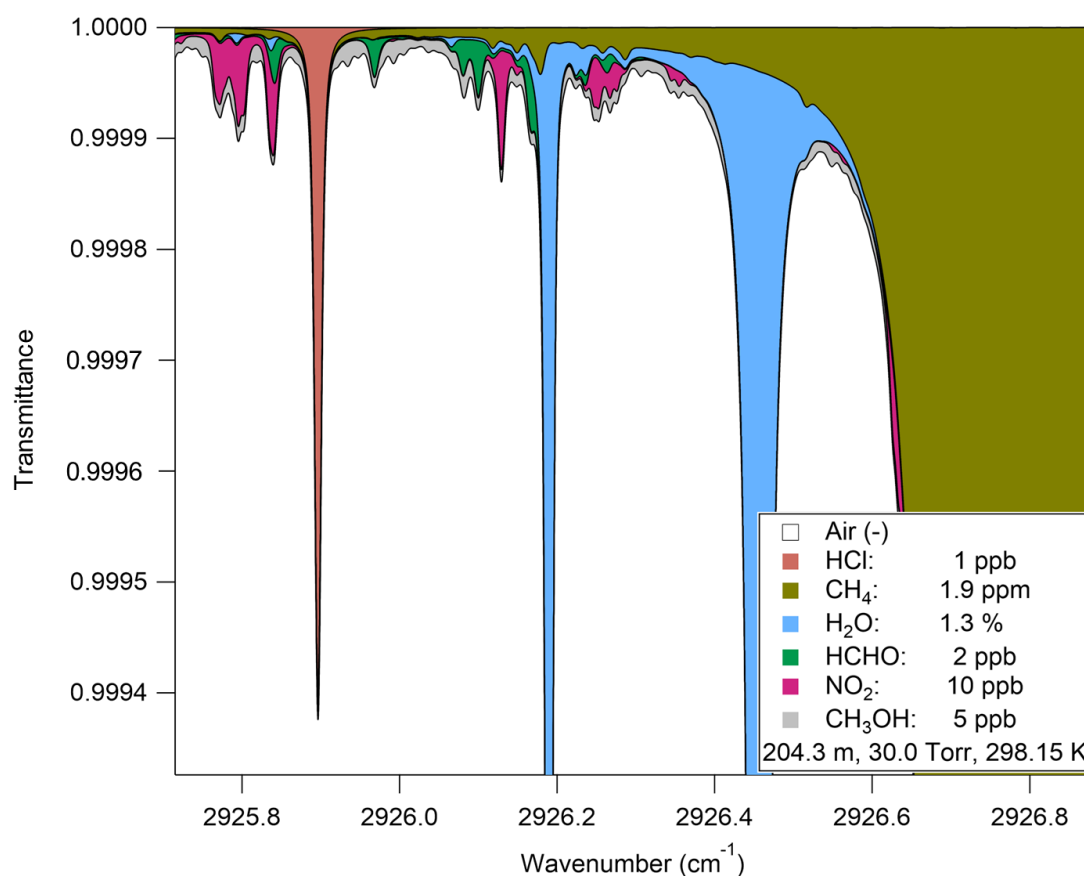
549



550 **Figure 10:** Time series of a) HCl when denuder was installed on HCl TILDAS inlet in comparison with b) pCl⁻
 551 observations. Available Cl was calculated by converting the pCl⁻ concentrations into mixing ratios. c) HCl cylinder
 552 additions were conducted (yellow shading) to verify the denuder was removing gas phase HCl. The data in panel c)
 553 has neither been blank corrected or time averaged.

554 4 Conclusions

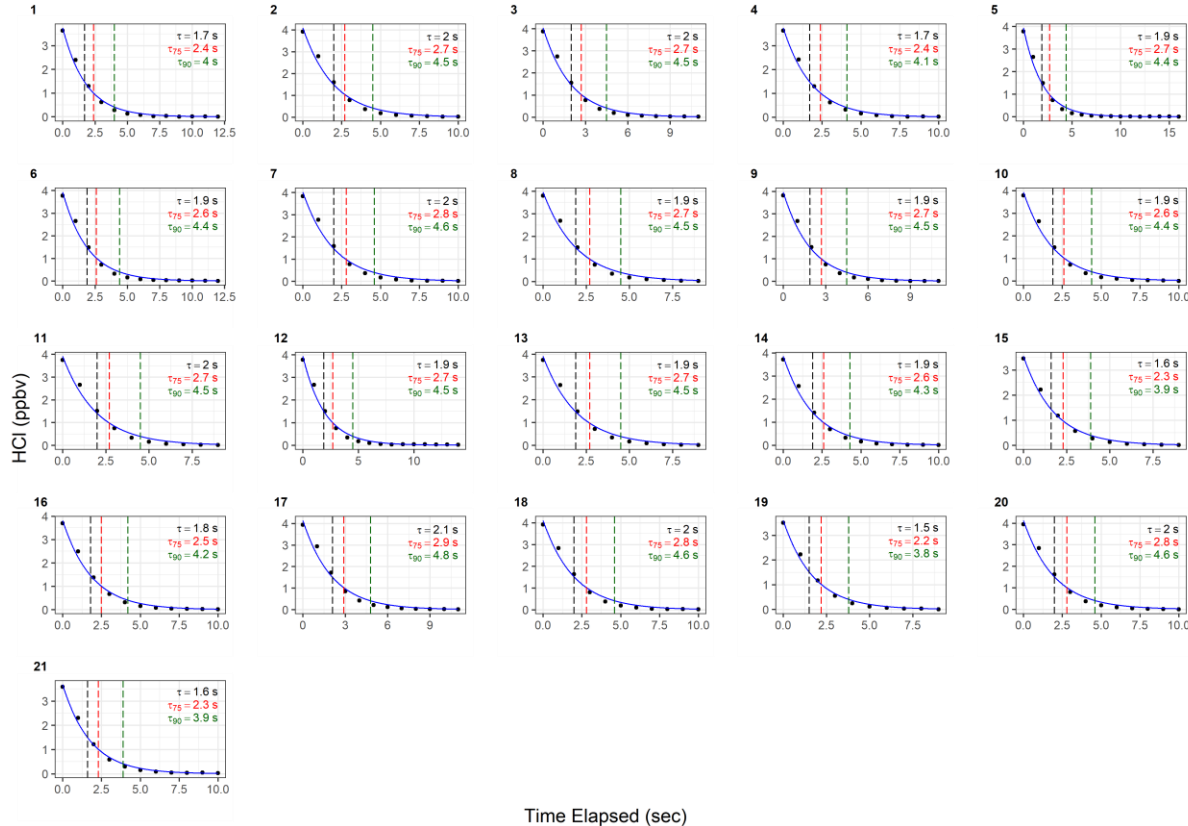
555 This work has demonstrated the viability of HCl-TILDAS for obtaining high-frequency ($\leq \sim 2\text{Hz}$) observations of
 556 ambient HCl. The associated sampling method, involving a virtual impactor to avoid excess surface-mediated
 557 interactions with filters, as well as heat and chemical passivation to increase HCl throughput, was also shown to
 558 greatly improve instrument response to changes in HCl concentration ($\tau_{90} \geq 1.15\text{ s}$). However, there is room for
 559 further innovation in obviating the stickiness of HCl, including additional heating of sampling lines, minimizing
 560 pressure within the sampling line, as well as utilizing higher flow inlets (e.g., $\geq 12\text{ L min}^{-1}$). The use of shorter
 561 inlet lines ($< 3\text{ m}$) operating at higher flow rates will additionally reduce sample air residence time in the inlet (\leq
 562 0.54 s , as in this study), both reducing HCl-wall interactions and mitigating the likelihood of HCl partitioning out
 563 of particulates within the inlet. **Introducing a temperature ramp to the inlet system after manual additions of high**
 564 **HCl mixing ratios may additionally reduce the amount of sorbed HCl available for acid displacement should**
 565 **strong acids be sampled under ambient conditions.** The fast time responses to changes in HCl mixing ratios shown
 566 herein will be well-suited for mobile sampling platforms, such as aircraft or vehicle-based laboratories, in which
 567 high temporal and spatial concentration variability are inherent. Finally, the potential for interferences from
 568 particulate chloride necessitates careful consideration for the method of obtaining background measurements.
 569 Regular installations of a denuder, or incorporation of a denuder into a background mechanism would minimize
 570 the uncertainty presented.

571 **Appendix A**572 **Figure A1** –HITRAN transmittance spectrum simulation demonstrating the separation of absorption peaks over the
573 observed spectral window (2925.80 to 2926.75 cm^{-1}).

574

575

Passivated HCl Decays (Dry)



576 **Figure A2 – Instrument response times to changes in HCl mixing ratios utilising active passivation. Black dots**
 577 **represent observed data and are overlayed by the calculated single exponential model (according to the terms listed in**
 578 **Table A1). Vertical hashed lines are placed on time elapsed corresponding to τ_e (black), τ_{75} (red), and τ_{90} (green).**

579
580 **Table A1 – Results for each model fit for determining the instrument response times under actively passivated**
581 **conditions with the 2.8 L min^{-1} inertial inlet, and corresponds with Fig. A2. Model parameters correspond to Eq. 1 in**
Sect. 2.6.2.

Trial	Single Exponential Fit					Bi-Exponential Fit								
	τ_e (s)	τ_{75} (s)	τ_{90} (s)	A_1	k_1	Residuals	τ_e (s)	τ_{75} (s)	τ_{90} (s)	A_1	k_1	A_2	k_2	Residuals
1	1.7	2.4	4	3.7 ± 0.1	0.58 ± 0.01	0.10	1.4	2.1	4	3.4 ± 1.2	0.8 ± 0.3	0.5 ± 1.2	0.2 ± 0.3	0.20
2	2	2.7	4.5	4.1 ± 0.1	0.60 ± 0.02	0.16	1.9	2.8	4.9	1.8 ± 10.4	0.8 ± 1.9	2.3 ± 10.4	0.4 ± 0.6	0.22
3	2	2.7	4.5	4.0 ± 0.1	0.60 ± 0.02	0.14	1.8	2.6	4.9	2.7 ± 4.1	0.8 ± 0.7	1.4 ± 4.1	0.3 ± 0.4	0.23
4	1.7	2.4	4.1	3.7 ± 0.1	0.58 ± 0.02	0.11	1.7	2.4	4.2	1.7 ± 12.1	0.8 ± 1.9	2.0 ± 12.1	0.4 ± 0.7	0.16
5	1.9	2.7	4.4	3.9 ± 0.1	0.60 ± 0.01	0.11	1.9	2.8	5	2.7 ± 4.1	0.7 ± 0.5	1.2 ± 4.2	0.3 ± 0.4	0.17
6	1.9	2.6	4.4	3.9 ± 0.1	0.60 ± 0.02	0.13	1.9	2.7	4.9	3.0 ± 4.2	0.6 ± 0.5	0.9 ± 4.2	0.3 ± 0.5	0.20
7	2	2.8	4.6	4.0 ± 0.2	0.60 ± 0.02	0.17	1.9	2.8	4.9	2.3 ± 10.3	0.7 ± 1.4	1.8 ± 10.3	0.3 ± 0.7	0.24
8	1.9	2.7	4.5	4.0 ± 0.1	0.60 ± 0.02	0.16	2	2.8	4.7	0.3 ± 21.3	0.8 ± 17.6	3.6 ± 21.3	0.5 ± 0.7	0.19
9	1.9	2.7	4.5	4.0 ± 0.1	0.60 ± 0.02	0.14	1.9	2.7	4.8	2.3 ± 5.6	0.8 ± 1.1	1.7 ± 5.6	0.3 ± 0.4	0.21
10	1.9	2.6	4.4	3.9 ± 0.1	0.60 ± 0.02	0.14	2	2.7	4.2	-4.5 ± 40.0	1.0 ± 1.6	8.3 ± 40.0 -1.1 ± 40.5	0.7 ± 0.5	0.09
11	2	2.7	4.5	3.9 ± 0.2	0.60 ± 0.02	0.16	2	2.7	4.5	4.9 ± 40.5	0.6 ± 0.9	0.8 ± 7.0	0.16	
12	1.9	2.7	4.5	3.9 ± 0.1	0.60 ± 0.02	0.12	1.6	2.2	4.2	3.8 ± 0.7	0.7 ± 0.2	0.3 ± 0.7	0.1 ± 0.2	0.26
13	1.9	2.7	4.5	3.9 ± 0.1	0.60 ± 0.02	0.16	2	2.8	4.6	-1.2 ± 54.2	0.8 ± 7.6	5.0 ± 54.2	0.5 ± 1.1	0.16
14	1.9	2.6	4.3	3.9 ± 0.1	0.59 ± 0.02	0.14	1.9	2.7	4.4	-0.1 ± 50.7	0.7 ± 79.7	3.9 ± 50.7	0.5 ± 1.2	0.15
15	1.6	2.3	3.9	3.5 ± 0.1	0.57 ± 0.02	0.10	1.6	2.3	4	-0.5 ± 48.7	0.8 ± 15.5	4.0 ± 48.7	0.6 ± 1.1	0.11
16	1.8	2.5	4.2	3.8 ± 0.1	0.59 ± 0.02	0.12	1.7	2.5	4.5	1.9 ± 8.7	0.8 ± 1.6	2.0 ± 8.8	0.4 ± 0.6	0.18
17	2.1	2.9	4.8	4.1 ± 0.2	0.62 ± 0.02	0.17	2.2	3	5	0.5 ± 23.4	0.8 ± 11.1	3.6 ± 23.4	0.4 ± 0.7	0.21
18	2	2.8	4.6	4.1 ± 0.2	0.61 ± 0.02	0.17	2	2.8	4.7	1.4 ± 39.6	0.4 ± 2.6	2.7 ± 39.5	0.6 ± 2.5	0.25
19	1.5	2.2	3.8	3.6 ± 0.1	0.56 ± 0.02	0.10	1.5	2.2	4	0.9 ± 9.3	0.9 ± 4.0	2.7 ± 9.3	0.5 ± 0.5	0.14
20	2	2.8	4.6	4.1 ± 0.2	0.60 ± 0.02	0.17								
21	1.6	2.3	3.9	3.7 ± 0.1	0.57 ± 0.01	0.09								

582

583

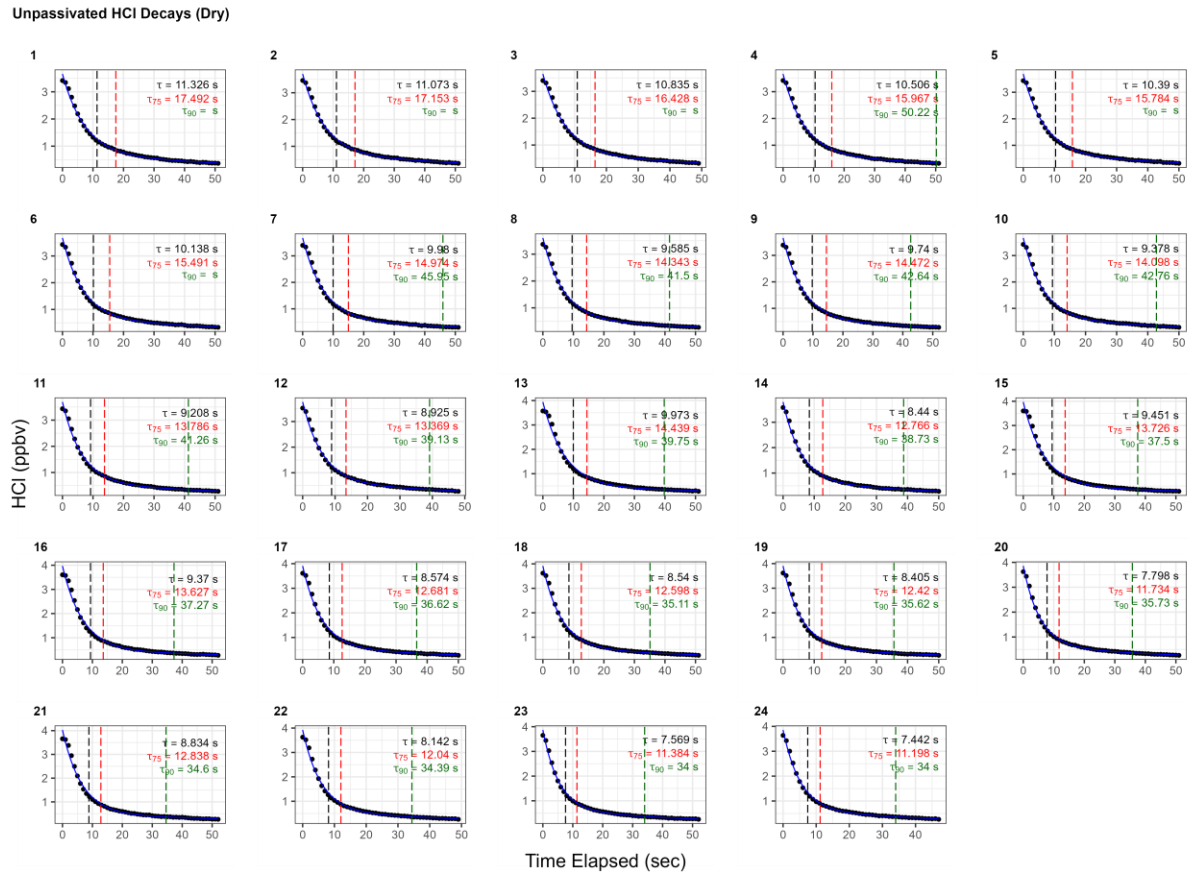


Figure A3 – Instrument response times to changes in HCl mixing ratios without active chemical passivation. Black dots represent observed data and are overlaid by the calculated bi-exponential model (according to the terms listed in Table A2). Vertical hashed lines are placed on time elapsed corresponding to τ_e (black), τ_{75} (red), and τ_{90} (green).

584

585
586
587

588

589 **Table A2 – Results for each model fit for determining the instrument response times without use of active chemical**
 590 **passivation, using the 2.8 L min⁻¹ inertial inlet, and corresponds with Fig. A3. Model parameters correspond to Eq. 1**
 591 **in Sect. 2.6.2.**

Trial	Single Exponential Fit						Bi-Exponential Fit							
	τ_e (s)	τ_{75} (s)	τ_{90} (s)	A_1	k_1	Residuals	τ_e (s)	τ_{75} (s)	τ_{90} (s)	A_1	k_1	A_2	k_2	Residuals
1	13.7	19.4	33	3.2 ± 0.1	0.935 ± 0.003	0.21	11.3	17.5		2.9 ± 0.1	0.136 ± 0.008	0.7 ± 0.1	0.013 ± 0.004	0.06
2	13.5	19.1	32.4	3.2 ± 0.1	0.933 ± 0.003	0.21	11.1	17.1		3.0 ± 0.1	0.139 ± 0.009	0.7 ± 0.1	0.012 ± 0.004	0.06
3	13	18.3	30.8	3.2 ± 0.1	0.930 ± 0.003	0.20	10.8	16.4		3.0 ± 0.1	0.140 ± 0.009	0.7 ± 0.1	0.014 ± 0.005	0.06
4	12.7	17.9	30.3	3.2 ± 0.1	0.929 ± 0.003	0.20	10.5	16		3.0 ± 0.1	0.142 ± 0.008	0.7 ± 0.1	0.014 ± 0.004	0.06
5	12.6	17.8	30.1	3.2 ± 0.1	0.928 ± 0.003	0.21	10.4	15.8		3.0 ± 0.1	0.143 ± 0.008	0.7 ± 0.1	0.013 ± 0.004	0.06
6	12.4	17.6	29.8	3.2 ± 0.1	0.928 ± 0.004	0.22	10.1	15.5		3.0 ± 0.1	0.148 ± 0.008	0.7 ± 0.1	0.013 ± 0.004	0.06
7	11.9	16.7	28.1	3.3 ± 0.1	0.923 ± 0.004	0.20	10	14.9		3.1 ± 0.1	0.144 ± 0.010	0.6 ± 0.1	0.011 ± 0.006	0.07
8	11.4	16	27.1	3.2 ± 0.1	0.920 ± 0.004	0.19	9.6	14.3	42.2	3.0 ± 0.1	0.150 ± 0.009	0.6 ± 0.1	0.014 ± 0.005	0.06
9	11.6	16.2	27.3	3.2 ± 0.1	0.920 ± 0.004	0.20	9.7	14.5	43.1	3.1 ± 0.1	0.147 ± 0.009	0.6 ± 0.1	0.012 ± 0.005	0.07
10	11.3	16	27.1	3.2 ± 0.1	0.921 ± 0.004	0.21	9.4	14.1	43.1	3.0 ± 0.1	0.155 ± 0.008	0.6 ± 0.1	0.014 ± 0.004	0.06
11	11	15.5	26.1	3.3 ± 0.1	0.918 ± 0.004	0.21	9.2	13.8	42.1	3.1 ± 0.1	0.156 ± 0.009	0.6 ± 0.1	0.014 ± 0.005	0.06
12	10.7	15.1	25.5	3.3 ± 0.1	0.916 ± 0.004	0.21	8.9	13.4	39.4	3.1 ± 0.1	0.162 ± 0.009	0.6 ± 0.1	0.016 ± 0.005	0.06
13	10.5	14.9	25.3	3.3 ± 0.1	0.916 ± 0.004	0.22	8.6	13	39.7	3.1 ± 0.1	0.169 ± 0.009	0.7 ± 0.1	0.016 ± 0.004	0.06
14	10.3	14.6	24.9	3.3 ± 0.1	0.915 ± 0.004	0.22	8.4	12.8	38.9	3.1 ± 0.1	0.172 ± 0.009	0.7 ± 0.1	0.017 ± 0.004	0.06
15	9.9	14.1	24.1	3.3 ± 0.1	0.912 ± 0.005	0.22	8.1	12.3	37.8	3.1 ± 0.1	0.181 ± 0.008	0.7 ± 0.1	0.018 ± 0.004	0.05
16	9.9	14.2	24.3	3.3 ± 0.1	0.913 ± 0.005	0.22	8	12.2	37.6	3.1 ± 0.1	0.181 ± 0.008	0.7 ± 0.1	0.018 ± 0.003	0.05
17	10.2	14.3	24.1	3.5 ± 0.1	0.910 ± 0.005	0.22	8.6	12.7	36.9	3.3 ± 0.1	0.164 ± 0.010	0.6 ± 0.1	0.013 ± 0.006	0.08
18	10.1	14.2	23.9	3.5 ± 0.1	0.910 ± 0.005	0.22	8.5	12.6	35.4	3.3 ± 0.1	0.163 ± 0.009	0.6 ± 0.1	0.013 ± 0.005	0.07
19	10	14.1	23.7	3.5 ± 0.1	0.909 ± 0.005	0.22	8.4	12.4	35.8	3.3 ± 0.1	0.167 ± 0.010	0.6 ± 0.1	0.014 ± 0.005	0.07
20	9.6	13.6	23.1	3.4 ± 0.1	0.908 ± 0.005	0.23	7.8	11.7	36	3.2 ± 0.1	0.184 ± 0.009	0.7 ± 0.1	0.017 ± 0.004	0.06
21	9.3	13.4	23	3.3 ± 0.1	0.909 ± 0.005	0.23	7.5	11.4	35.4	3.1 ± 0.1	0.192 ± 0.007	0.7 ± 0.1	0.018 ± 0.003	0.05
22	9.7	13.7	23	3.5 ± 0.1	0.907 ± 0.005	0.23	8.1	12	34.4	3.3 ± 0.1	0.173 ± 0.010	0.6 ± 0.1	0.015 ± 0.005	0.08
23	9.2	13.1	22.2	3.4 ± 0.1	0.904 ± 0.005	0.22	7.6	11.4	34.2	3.2 ± 0.1	0.189 ± 0.010	0.7 ± 0.1	0.018 ± 0.005	0.06
24	9.1	13	22.1	3.4 ± 0.1	0.904 ± 0.005	0.23	7.4	11.2	34	3.2 ± 0.1	0.192 ± 0.009	0.7 ± 0.1	0.018 ± 0.004	0.06

592
593

Passivated HCl Decays (Dry)

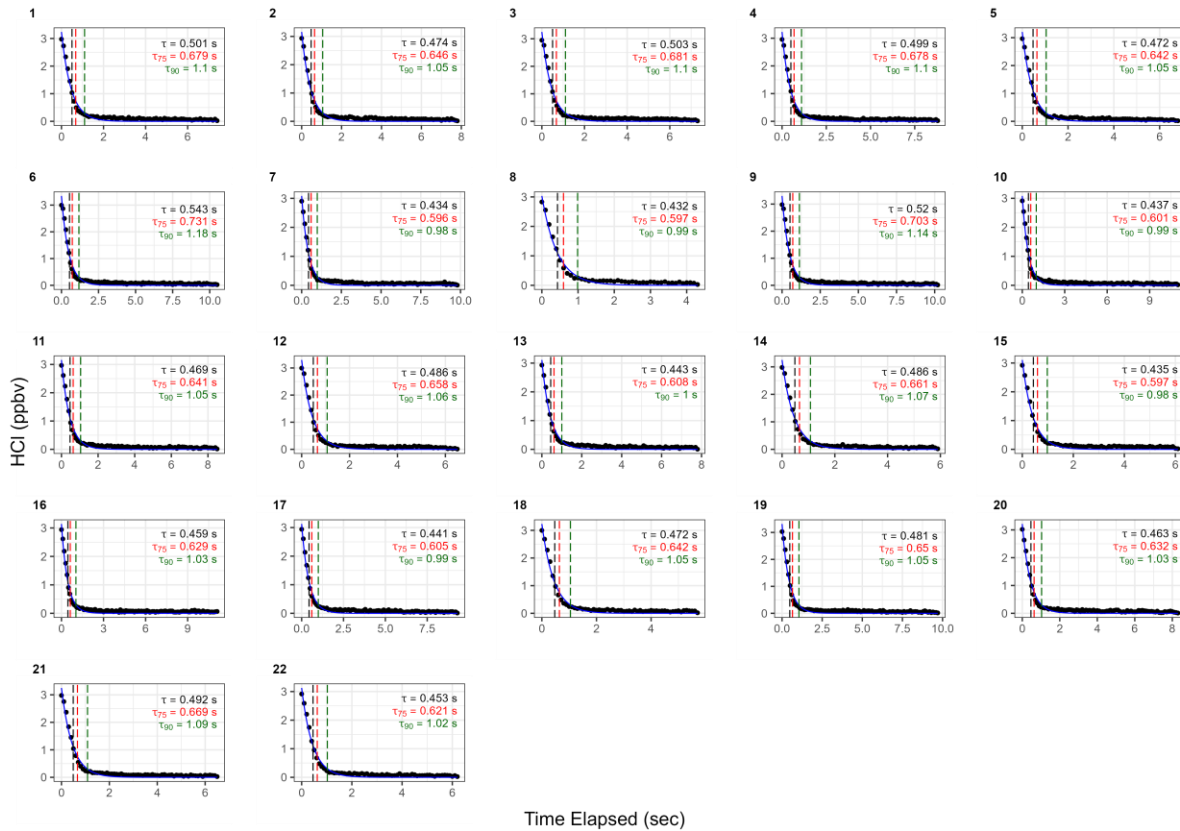


Figure A4: Instrument response times to changes in HCl mixing ratios with active chemical passivation and a high flow inertial inlet (12.7 L min⁻¹). Black dots represent observed data and are overlaid by the calculated single exponential model (according to the terms listed in Table A3). Vertical hashed lines are placed on time elapsed corresponding to τ_e (black), τ_{75} (red), and τ_{90} (green).

594
595
596
597

598 **Table A3: Results for each model fit for determining the instrument response times under actively passivated conditions**
 599 **with the 12.7 L min⁻¹ inertial inlet (Fig. A4). Model parameters correspond to Eq. 1 in Sect. 2.6.2.**

Trial	Single Exponential Fit					
	τ_e (s)	τ_{75} (s)	τ_{90} (s)	A_1	k_1	Residuals
1	0.50	0.68	1.10	3.24 ± 0.08	0.113 ± 0.009	0.10
2	0.47	0.65	1.06	3.16 ± 0.08	0.106 ± 0.009	0.10
3	0.50	0.68	1.11	3.25 ± 0.08	0.12 ± 0.01	0.10
4	0.50	0.68	1.10	3.22 ± 0.07	0.115 ± 0.009	0.09
5	0.47	0.64	1.05	3.21 ± 0.08	0.103 ± 0.009	0.10
6	0.54	0.73	1.18	3.34 ± 0.07	0.129 ± 0.009	0.10
7	0.43	0.60	0.98	3.08 ± 0.06	0.093 ± 0.007	0.08
8	0.43	0.60	0.99	3.03 ± 0.08	0.10 ± 0.01	0.11
9	0.52	0.70	1.14	3.30 ± 0.07	0.121 ± 0.009	0.10
10	0.44	0.60	0.99	3.08 ± 0.06	0.095 ± 0.007	0.08
11	0.47	0.64	1.05	3.16 ± 0.07	0.106 ± 0.008	0.09
12	0.49	0.66	1.07	3.30 ± 0.08	0.105 ± 0.009	0.11
13	0.44	0.61	1.00	3.11 ± 0.07	0.097 ± 0.008	0.09
14	0.49	0.66	1.08	3.25 ± 0.08	0.109 ± 0.009	0.10
15	0.44	0.60	0.98	3.10 ± 0.08	0.092 ± 0.008	0.10
16	0.46	0.63	1.03	3.14 ± 0.06	0.103 ± 0.007	0.08
17	0.44	0.61	0.99	3.13 ± 0.07	0.095 ± 0.008	0.09
18	0.47	0.64	1.05	3.23 ± 0.08	0.104 ± 0.009	0.10
19	0.48	0.65	1.05	3.32 ± 0.07	0.102 ± 0.008	0.09
20	0.46	0.63	1.03	3.21 ± 0.07	0.101 ± 0.008	0.09
21	0.49	0.67	1.09	3.25 ± 0.07	0.112 ± 0.009	0.10
22	0.45	0.62	1.02	3.13 ± 0.07	0.101 ± 0.008	0.09

600

601

602 **Acknowledgements**

603 This program of work was primarily supported by the European Research Council (ERC-StG 802685). The
604 Aerodyne Research Inc. HCl instrument development work was funded by the NOAA Small Business Innovation
605 Research Program (WC-133R-17-CN-0092), and the Manchester field measurements were supported by the
606 NERC SPF OSCA project (NE/T001917/1). The authors would also like to thank Abigail Mortimer, Stuart
607 Murray, Chris Rhodes, and Mark Roper in the University of York Chemistry workshops, as well as Christopher
608 Anthony, for technical support, and Stuart Lacy in the University of York Wolfson Atmospheric Chemistry
609 Laboratory for data analysis software support. Further, the authors thank Michael Agnese and Michael Moore for
610 TILDAS technical support. The authors would like to acknowledge the efforts Conner Daube made in testing
611 configuration and sampling procedures on the companion HCl instrument. The author would also like to
612 acknowledge the spectroscopic analysis performed by J. Barry McManus to diagnose non-ideal noise sources and
613 design alignment optimizations. In addition, the authors thank James Lee, Will Drysdale, and Katie Read for their
614 support in laboratory experiments involving HNO₃ quantification.

615 **Code availability**

616 ~~The code used to perform the calculations used in this study will be made publicly available on completion of the~~
617 ~~review process. In the meantime, data~~ Code used for this study can be obtained from the corresponding author
618 upon request.

619 **Data availability**

620 ~~The data used in this study will be made publicly available on completion of the review process. In the meantime,~~
621 ~~data~~ Data used for this study can be obtained from the corresponding author upon request.

622 **Author contribution**

623 SCH, JRR, CD, and TIY designed, built, and tested the HCl TILDAS at Aerodyne Research, Inc. SSB and PRV
624 were involved in the initial HCl detector testing and support of Aerodyne Research, Inc., instrument development.
625 JWH and PME designed laboratory and field experiments, and JWH conducted laboratory and field experiments.
626 SJA designed and constructed bespoke temperature controlling units for the inertial inlet, the field inlet box, and
627 permeation source ovens. JS performed ISOROPPIA modelling experiments. MF provided NO_x and NO_y data,
628 as well as provided critical field support during the OSCA campaign. JWH prepared the manuscript, and all
629 authors reviewed the manuscript.

630 **Competing interests**

631 The authors declare that they have no conflict of interest.

632 **References**

633 Abbatt, J., Oldridge, N., Symington, A., Chukalovskiy, V., McWhinney, R. D., Sjostedt, S., and Cox, R. A.:
 634 Release of Gas-Phase Halogens by Photolytic Generation of OH in Frozen Halide–Nitrate Solutions: An Active
 635 Halogen Formation Mechanism?, *J. Phys. Chem. A*, 114, 6527–6533, <https://doi.org/10.1021/jp102072t>, 2010.

636 Allan, W., Lowe, D. C., and Cainey, J. M.: Active chlorine in the remote marine boundary layer: Modeling
 637 anomalous measurements of $\delta^{13}\text{C}$ in methane, *Geophys. Res. Lett.*, 28, 3239–3242,
 638 <https://doi.org/10.1029/2001GL013064>, 2001.

639 Angelucci, A. A., Furlani, T. C., Wang, X., Jacob, D. J., VandenBoer, T. C., and Young, C. J.: Understanding
 640 Sources of Atmospheric Hydrogen Chloride in Coastal Spring and Continental Winter, *ACS Earth Space Chem.*,
 641 5, 2507–2516, <https://doi.org/10.1021/acsearthspacechem.1c00193>, 2021.

642 Atkinson, R., Baulch, D. L., Cox, R. A., Crowley, J. N., Hampson, R. F., Hynes, R. G., Jenkin, M. E., Rossi, M.
 643 J., Troe, J., and IUPAC Subcommittee: Evaluated kinetic and photochemical data for atmospheric chemistry:
 644 Volume II - gas phase reactions of organic species, *Atmospheric Chem. Phys.*, 6, 3625–4055,
 645 <https://doi.org/10.5194/acp-6-3625-2006>, 2006.

646 Atkinson, R., Baulch, D. L., Cox, R. A., Crowley, J. N., Hampson, R. F., Hynes, R. G., Jenkin, M. E., Rossi, M.
 647 J., and Troe, J.: Evaluated kinetic and photochemical data for atmospheric chemistry: Volume III - gas phase
 648 reactions of inorganic halogens, *Atmospheric Chem. Phys.*, 7, 981–1191, <https://doi.org/10.5194/acp-7-981-2007>,
 649 2007.

650 Bandy, B., Faloon, K., Finessi, E., Lee, J. D., Leigh, R. J., Liu, D., Monks, P. S., Oram, D. E., Visser, S.,
 651 Whitehead, J., and Young, D.: ClearfLo: IOP Summer Atmospheric Chemistry and meteorology measurements
 652 and NAME Airmass Footprint dispersion model output at North Kensington, London, CAS Br. Atmospheric Data
 653 Cent., <https://catalogue.ceda.ac.uk/uuid/4c35e63d6507408d96e4af3dce410e3d>, 2022a.

654 Bandy, B., Faloon, K., Finessi, E., Herndon, S. C., Laufs, S., Lee, J. D., Leigh, R. J., Liu, D., Monks, P. S., Oram,
 655 D. E., Visser, S., Whitehead, J., Young, D., and Zotter, P.: ClearfLo: Longterm atmospheric chemistry and
 656 meteorological measurements and NAME dispersion model output for ClearfLo, CAS Br. Atmospheric Data
 657 Cent., <https://catalogue.ceda.ac.uk/uuid/f02d656eddf44f4283c085fc763a6f02>, 2022b.

658 Behnke, W. and Zetzs, C.: Heterogeneous photochemical formation of Cl atoms from NaCl aerosol, NO_x and
 659 ozone, *J. Aerosol Sci.*, 21, S229–S232, [https://doi.org/10.1016/0021-8502\(90\)90226-N](https://doi.org/10.1016/0021-8502(90)90226-N), 1990.

660 Behnke, W., Krüger, H.-U., Scheer, V., and Zetzs, C.: Formation of ClNO_2 and hono in the presence of NO_2 ,
 661 O_3 and wet NaCl aerosol, *J. Aerosol Sci.*, 23, 933–936, [https://doi.org/10.1016/0021-8502\(92\)90565-D](https://doi.org/10.1016/0021-8502(92)90565-D), 1992.

662 Behnke, W., George, C., Scheer, V., and Zetzs, C.: Production and decay of ClNO_2 from the reaction of gaseous
 663 N_2O_5 with NaCl solution: Bulk and aerosol experiments, *J. Geophys. Res. Atmospheres*, 102, 3795–3804,
 664 <https://doi.org/10.1029/96JD03057>, 1997.

665 Beichert, P. and Finlayson-Pitts, B. J.: Knudsen Cell Studies of the Uptake of Gaseous HNO_3 and Other Oxides
 666 of Nitrogen on Solid NaCl: The Role of Surface-Adsorbed Water, *J. Phys. Chem.*, 100, 15218–15228,
 667 <https://doi.org/10.1021/jp960925u>, 1996.

668 Brimblecombe, P. and Clegg, S. L.: The solubility and behaviour of acid gases in the marine aerosol, *J.
 669 Atmospheric Chem.*, 7, 1–18, <https://doi.org/10.1007/BF00048251>, 1988.

670 Buck, R. C., Franklin, J., Berger, U., Conder, J. M., Cousins, I. T., de Voogt, P., Jensen, A. A., Kannan, K.,
 671 Mabury, S. A., and van Leeuwen, S. P.: Perfluoroalkyl and polyfluoroalkyl substances in the environment:

672 Terminology, classification, and origins, *Integr. Environ. Assess. Manag.*, 7, 513–541,
673 <https://doi.org/10.1002/ieam.258>, 2011.

674 Burkholder, J. B., Sander, S. P., Abbatt, J., Barker, J. R., Huie, R. E., Kolb, C. E., Kurylo, M. J., Orkin, V. L.,
675 Wilmouth, D. M., and Wine, P. H.: Chemical Kinetics and Photochemical Data for Use in Atmospheric Studies,
676 Evaluation No. 18, JPL Publication 15-10., Jet Propulsion Laboratory, Pasadena, 2015.

677 Clegg, S. L. and Brimblecombe, P.: The dissociation constant and henry's law constant of HCl in aqueous solution,
678 *Atmospheric Environ.* 1967, 20, 2483–2485, [https://doi.org/10.1016/0004-6981\(86\)90079-X](https://doi.org/10.1016/0004-6981(86)90079-X), 1986.

679 Crilley, L. R., Lucarelli, F., Bloss, W. J., Harrison, R. M., Beddows, D. C., Calzolai, G., Nava, S., Valli, G.,
680 Bernardoni, V., and Vecchi, R.: Source apportionment of fine and coarse particles at a roadside and urban
681 background site in London during the 2012 summer ClearfLo campaign, *Environ. Pollut.*, 220, 766–778,
682 <https://doi.org/10.1016/j.envpol.2016.06.002>, 2017.

683 Crisp, T. A., Lerner, B. M., Williams, E. J., Quinn, P. K., Bates, T. S., and Bertram, T. H.: Observations of gas
684 phase hydrochloric acid in the polluted marine boundary layer, *J. Geophys. Res. Atmospheres*, 119, 6897–6915,
685 <https://doi.org/10.1002/2013JD020992>, 2014.

686 Eger, P. G., Helleis, F., Schuster, G., Phillips, G. J., Lelieveld, J., and Crowley, J. N.: Chemical ionization
687 quadrupole mass spectrometer with an electrical discharge ion source for atmospheric trace gas measurement,
688 *Atmospheric Meas. Tech.*, 12, 1935–1954, <https://doi.org/10.5194/amt-12-1935-2019>, 2019a.

689 Eger, P. G., Friedrich, N., Schuladen, J., Shenolikar, J., Fischer, H., Tadic, I., Harder, H., Martinez, M., Rohloff,
690 R., Tauer, S., Drewnick, F., Fachinger, F., Brooks, J., Darbyshire, E., Sciare, J., Pikridas, M., Lelieveld, J., and
691 Crowley, J. N.: Shipborne measurements of ClNO₂ in the Mediterranean Sea and around the Arabian Peninsula
692 during summer, *Atmospheric Chem. Phys.*, 19, 12121–12140, <https://doi.org/10.5194/acp-19-12121-2019>,
693 2019b.

694 Ellis, R. A., Murphy, J. G., Pattey, E., van Haarlem, R., O'Brien, J. M., and Herndon, S. C.: Characterizing a
695 Quantum Cascade Tunable Infrared Laser Differential Absorption Spectrometer (QC-TILDAS) for measurements
696 of atmospheric ammonia, *Atmospheric Meas. Tech.*, 3, 397–406, <https://doi.org/10.5194/amt-3-397-2010>, 2010.

697 Erickson, D. J., Seuzaret, C., Keene, W. C., and Gong, S. L.: A general circulation model based calculation of
698 HCl and ClNO₂ production from sea salt dechlorination: Reactive Chlorine Emissions Inventory, *J. Geophys. Res.*
699 *Atmospheres*, 104, 8347–8372, <https://doi.org/10.1029/98JD01384>, 1999.

700 Fickert, S., Adams, J. W., and Crowley, J. N.: Activation of Br₂ and BrCl via uptake of HOBr onto aqueous salt
701 solutions, *J. Geophys. Res. Atmospheres*, 104, 23719–23727, <https://doi.org/10.1029/1999JD900359>, 1999.

702 Fountoukis, C. and Nenes, A.: ISORROPIA II: a computationally efficient thermodynamic equilibrium model for
703 K⁺-Ca²⁺-Mg²⁺-NH₄⁺-Na⁺-SO₄²⁻-NO₃⁻-Cl⁻H₂O aerosols, *Atmospheric Chem. Phys.*, 7, 4639–4659,
704 <https://doi.org/10.5194/acp-7-4639-2007>, 2007.

705 Frinak, E. K. and Abbatt, J. P. D.: Br₂ Production from the Heterogeneous Reaction of Gas-Phase OH with
706 Aqueous Salt Solutions: Impacts of Acidity, Halide Concentration, and Organic Surfactants, *J. Phys. Chem. A*,
707 110, 10456–10464, <https://doi.org/10.1021/jp063165o>, 2006.

708 Fu, X., Wang, T., Wang, S., Zhang, L., Cai, S., Xing, J., and Hao, J.: Anthropogenic Emissions of Hydrogen
709 Chloride and Fine Particulate Chloride in China, *Environ. Sci. Technol.*, 52, 1644–1654,
710 <https://doi.org/10.1021/acs.est.7b05030>, 2018.

711 Furlani, T. C., Veres, P. R., Dawe, K. E. R., Neuman, J. A., Brown, S. S., VandenBoer, T. C., and Young, C. J.:
712 Validation of a new cavity ring-down spectrometer for measuring tropospheric gaseous hydrogen chloride,
713 *Atmospheric Meas. Tech.*, 14, 5859–5871, <https://doi.org/10.5194/amt-14-5859-2021>, 2021.

714 von Glasow, R., Bobrowski, N., and Kern, C.: The effects of volcanic eruptions on atmospheric chemistry, *Chem.*
715 *Geol.*, 263, 131–142, <https://doi.org/10.1016/j.chemgeo.2008.08.020>, 2009.

716 Gordon, I. E., Rothman, L. S., Hill, C., Kochanov, R. V., Tan, Y., Bernath, P. F., Birk, M., Boudon, V.,
717 Campargue, A., Chance, K. V., Drouin, B. J., Flaud, J.-M., Gamache, R. R., Hodges, J. T., Jacquemart, D.,
718 Perevalov, V. I., Perrin, A., Shine, K. P., Smith, M.-A. H., Tennyson, J., Toon, G. C., Tran, H., Tyuterev, V. G.,
719 Barbe, A., Császár, A. G., Devi, V. M., Furtenbacher, T., Harrison, J. J., Hartmann, J.-M., Jolly, A., Johnson, T.
720 J., Karman, T., Kleiner, I., Kyuberis, A. A., Loos, J., Lyulin, O. M., Massie, S. T., Mikhailenko, S. N., Moazzen-
721 Ahmadi, N., Müller, H. S. P., Naumenko, O. V., Nikitin, A. V., Polyansky, O. L., Rey, M., Rotger, M., Sharpe,
722 S. W., Sung, K., Starikova, E., Tashkun, S. A., Auwera, J. V., Wagner, G., Wilzewski, J., Wcisło, P., Yu, S., and
723 Zak, E. J.: The HITRAN2016 molecular spectroscopic database, *J. Quant. Spectrosc. Radiat. Transf.*, 203, 3–69,
724 <https://doi.org/10.1016/j.jqsrt.2017.06.038>, 2017.

725 Graedel, T. E. and Keene, W. C.: Tropospheric budget of reactive chlorine, *Glob. Biogeochem. Cycles*, 9, 47–77,
726 <https://doi.org/10.1029/94GB03103>, 1995.

727 Graedel, T. E. and Keene, W. C.: The Budget and Cycle of Earth's Natural Chlorine, *Pure Appl. Chem.*, 68, 1689–
728 1697, <https://doi.org/10.1351/pac199668091689>, 1996.

729 Hagen, C. L., Lee, B. C., Franka, I. S., Rath, J. L., VandenBoer, T. C., Roberts, J. M., Brown, S. S., and Yalin, A.
730 P.: Cavity ring-down spectroscopy sensor for detection of hydrogen chloride, *Atmospheric Meas. Tech.*, 7, 345–
731 357, <https://doi.org/10.5194/amt-7-345-2014>, 2014.

732 Harris, G. W., Klemp, D., and Zenker, T.: An upper limit on the HCl near-surface mixing ratio over the Atlantic
733 measured using TDLAS, *J. Atmospheric Chem.*, 15, 327–332, <https://doi.org/10.1007/BF00115402>, 1992.

734 Haskins, J. D., Jaeglé, L., Shah, V., Lee, B. H., Lopez-Hilfiker, F. D., Campuzano-Jost, P., Schroder, J. C., Day,
735 D. A., Guo, H., Sullivan, A. P., Weber, R., Dibb, J., Campos, T., Jimenez, J. L., Brown, S. S., and Thornton, J.
736 A.: Wintertime Gas-Particle Partitioning and Speciation of Inorganic Chlorine in the Lower Troposphere Over
737 the Northeast United States and Coastal Ocean, *J. Geophys. Res. Atmospheres*, 123, 12,897–12,916,
738 <https://doi.org/10.1029/2018JD028786>, 2018.

739 Huffman, J. A., Docherty, K. S., Aiken, A. C., Cubison, M. J., Ulbrich, I. M., DeCarlo, P. F., Sueper, D., Jayne,
740 J. T., Worsnop, D. R., Ziemann, P. J., and Jimenez, J. L.: Chemically-resolved aerosol volatility measurements
741 from two megacity field studies, *Atmospheric Chem. Phys.*, 9, 7161–7182, <https://doi.org/10.5194/acp-9-7161-2009>, 2009.

742 Jahn, L. G., Wang, D. S., Dhulipala, S. V., and Ruiz, L. H.: Gas-Phase Chlorine Radical Oxidation of Alkanes:
743 Effects of Structural Branching, NO_x, and Relative Humidity Observed during Environmental Chamber
744 Experiments, *J. Phys. Chem. A*, 125, 7303–7317, <https://doi.org/10.1021/acs.jpca.1c03516>, 2021.

745 Keene, W. C., Khalil, M. A. K., Erickson, D. J., McCulloch, A., Graedel, T. E., Lobert, J. M., Aucott, M. L.,
746 Gong, S. L., Harper, D. B., Kleiman, G., Midgley, P., Moore, R. M., Seuzaret, C., Sturges, W. T., Benkovitz, C.
747 M., Koropalov, V., Barrie, L. A., and Li, Y. F.: Composite global emissions of reactive chlorine from
748 anthropogenic and natural sources: Reactive Chlorine Emissions Inventory, *J. Geophys. Res. Atmospheres*, 104,
749 8429–8440, <https://doi.org/10.1029/1998JD100084>, 1999.

751 Knipping, E. M., Lakin, M. J., Foster, K. L., Jungwirth, P., Tobias, D. J., Gerber, R. B., Dabdub, D., and Finlayson-
752 Pitts, B. J.: Experiments and Simulations of Ion-Enhanced Interfacial Chemistry on Aqueous NaCl Aerosols,
753 *Science*, 288, 301–306, <https://doi.org/10.1126/science.288.5464.301>, 2000.

754 Laasonen, K. E. and Klein, M. L.: Ab Initio Study of Aqueous Hydrochloric Acid, *J. Phys. Chem. A*, 101, 98–
755 102, <https://doi.org/10.1021/jp962513r>, 1997.

756 Laskin, A., Moffet, R. C., Gilles, M. K., Fast, J. D., Zaveri, R. A., Wang, B., Nigge, P., and Shutthanandan, J.:
757 Tropospheric chemistry of internally mixed sea salt and organic particles: Surprising reactivity of NaCl with weak
758 organic acids, *J. Geophys. Res. Atmospheres*, 117, <https://doi.org/10.1029/2012JD017743>, 2012.

759 Lee, B. H., Lopez-Hilfiker, F. D., Schroder, J. C., Campuzano-Jost, P., Jimenez, J. L., McDuffie, E. E., Fibiger,
760 D. L., Veres, P. R., Brown, S. S., Campos, T. L., Weinheimer, A. J., Flocke, F. F., Norris, G., O'Mara, K., Green,
761 J. R., Fiddler, M. N., Bililign, S., Shah, V., Jaeglé, L., and Thornton, J. A.: Airborne Observations of Reactive
762 Inorganic Chlorine and Bromine Species in the Exhaust of Coal-Fired Power Plants, *J. Geophys. Res. Atmospheres*, 123,
763 11,225–11,237, <https://doi.org/10.1029/2018JD029284>, 2018.

764 Li, G., Gordon, I. E., Bernath, P. F., and Rothman, L. S.: Direct fit of experimental ro-vibrational intensities to
765 the dipole moment function: Application to HCl, *J. Quant. Spectrosc. Radiat. Transf.*, 112, 1543–1550,
766 <https://doi.org/10.1016/j.jqsrt.2011.03.014>, 2011.

767 Li, G., Gordon, I. E., Hajigeorgiou, P. G., Coxon, J. A., and Rothman, L. S.: Reference spectroscopic data for
768 hydrogen halides, Part II: The line lists, *J. Quant. Spectrosc. Radiat. Transf.*, 130, 284–295,
769 <https://doi.org/10.1016/j.jqsrt.2013.07.019>, 2013.

770 Liao, J., Huey, L. G., Liu, Z., Tanner, D. J., Cantrell, C. A., Orlando, J. J., Flocke, F. M., Shepson, P. B.,
771 Weinheimer, A. J., Hall, S. R., Ullmann, K., Beine, H. J., Wang, Y., Ingall, E. D., Stephens, C. R., Hornbrook, R.
772 S., Apel, E. C., Riemer, D., Fried, A., Mauldin Iii, R. L., Smith, J. N., Staebler, R. M., Neuman, J. A., and Nowak,
773 J. B.: High levels of molecular chlorine in the Arctic atmosphere, *Nat. Geosci.*, 7, 91–94,
774 <https://doi.org/10.1038/ngeo2046>, 2014.

775 Liu, X., Deming, B., Pagonis, D., Day, D. A., Palm, B. B., Talukdar, R., Roberts, J. M., Veres, P. R., Krechmer,
776 J. E., Thornton, J. A., de Gouw, J. A., Ziemann, P. J., and Jimenez, J. L.: Effects of gas–wall interactions on
777 measurements of semivolatile compounds and small polar molecules, *Atmospheric Meas. Tech.*, 12, 3137–3149,
778 <https://doi.org/10.5194/amt-12-3137-2019>, 2019.

779 Marcy, T. P., Fahey, D. W., Gao, R. S., Popp, P. J., Richard, E. C., Thompson, T. L., Rosenlof, K. H., Ray, E. A.,
780 Salawitch, R. J., Atherton, C. S., Bergmann, D. J., Ridley, B. A., Weinheimer, A. J., Loewenstein, M., Weinstock,
781 E. M., and Mahoney, M. J.: Quantifying Stratospheric Ozone in the Upper Troposphere with in Situ Measurements
782 of HCl, *Science*, 304, 261–265, <https://doi.org/10.1126/science.1093418>, 2004.

783 McCulloch, A., Aucott, M. L., Benkovitz, C. M., Graedel, T. E., Kleiman, G., Midgley, P. M., and Li, Y.-F.:
784 Global emissions of hydrogen chloride and chloromethane from coal combustion, incineration and industrial
785 activities: Reactive Chlorine Emissions Inventory, *J. Geophys. Res. Atmospheres*, 104, 8391–8403,
786 <https://doi.org/10.1029/1999JD900025>, 1999.

787 McManus, J. B., Zahniser, M. S., and Nelson, D. D.: Dual quantum cascade laser trace gas instrument with
788 astigmatic Herriott cell at high pass number, *Appl. Opt.*, 50, A74, <https://doi.org/10.1364/AO.50.000A74>, 2011.

789 McManus, J. B., Zahniser, M. S., Nelson, D. D., Shorter, J. H., Herndon, S. C., Jervis, D., Agnese, M., McGovern,
790 R., Yacovitch, T. I., and Roscioli, J. R.: Recent progress in laser-based trace gas instruments: performance and
791 noise analysis, *Appl. Phys. B*, 119, 203–218, <https://doi.org/10.1007/s00340-015-6033-0>, 2015.

792 Neuman, J. A., Huey, L. G., Ryerson, T. B., and Fahey, D. W.: Study of Inlet Materials for Sampling Atmospheric
793 Nitric Acid, *Environ. Sci. Technol.*, 33, 1133–1136, <https://doi.org/10.1021/es980767f>, 1999.

794 Osthoff, H. D., Roberts, J. M., Ravishankara, A. R., Williams, E. J., Lerner, B. M., Sommariva, R., Bates, T. S.,
795 Coffman, D., Quinn, P. K., Dibb, J. E., Stark, H., Burkholder, J. B., Talukdar, R. K., Meagher, J., Fehsenfeld, F.
796 C., and Brown, S. S.: High levels of nitryl chloride in the polluted subtropical marine boundary layer, *Nat. Geosci.*,
797 1, 324–328, <https://doi.org/10.1038/ngeo177>, 2008.

798 Oum, K. W., Lakin, M. J., DeHaan, D. O., Brauers, T., and Finlayson-Pitts, B. J.: Formation of Molecular Chlorine
799 from the Photolysis of Ozone and Aqueous Sea-Salt Particles, *Science*, 279, 74–76,
800 <https://doi.org/10.1126/science.279.5347.74>, 1998.

801 Pollack, I. B., Lindaas, J., Roscioli, J. R., Agnese, M., Permar, W., Hu, L., and Fischer, E. V.: Evaluation of
802 ambient ammonia measurements from a research aircraft using a closed-path QC-TILDAS operated with active
803 continuous passivation, *Atmospheric Meas. Tech.*, 12, 3717–3742, <https://doi.org/10.5194/amt-12-3717-2019>,
804 2019.

805 Pszenny, A. A. P., Fischer, E. V., Russo, R. S., Sive, B. C., and Varner, R. K.: Estimates of Cl atom concentrations
806 and hydrocarbon kinetic reactivity in surface air at Appledore Island, Maine (USA), during International
807 Consortium for Atmospheric Research on Transport and Transformation/Chemistry of Halogens at the Isles of
808 Shoals, *J. Geophys. Res. Atmospheres*, 112, <https://doi.org/10.1029/2006JD007725>, 2007.

809 R Core Team: R: A language and environment for statistical computing., 2021.

810 Ren, X., Sun, R., Chi, H.-H., Meng, X., Li, Y., and Levendis, Y. A.: Hydrogen chloride emissions from
811 combustion of raw and torrefied biomass, *Fuel*, 200, 37–46, <https://doi.org/10.1016/j.fuel.2017.03.040>, 2017.

812 Roberts, J. M., Veres, P., Warneke, C., Neuman, J. A., Washenfelder, R. A., Brown, S. S., Baasandorj, M.,
813 Burkholder, J. B., Burling, I. R., Johnson, T. J., Yokelson, R. J., and de Gouw, J.: Measurement of HONO, HNCO,
814 and other inorganic acids by negative-ion proton-transfer chemical-ionization mass spectrometry (NI-PT-CIMS):
815 application to biomass burning emissions, *Atmospheric Meas. Tech.*, 3, 981–990, <https://doi.org/10.5194/amt-3-981-2010>, 2010.

817 Roscioli, J. R., Zahniser, M. S., Nelson, D. D., Herndon, S. C., and Kolb, C. E.: New Approaches to Measuring
818 Sticky Molecules: Improvement of Instrumental Response Times Using Active Passivation, *J. Phys. Chem. A*,
819 120, 1347–1357, <https://doi.org/10.1021/acs.jpca.5b04395>, 2016.

820 RStudio Team: RStudio: Integrated Development Environment for R, 2021.

821 Saliba, N. A., Yang, H., and Finlayson-Pitts, B. J.: Reaction of Gaseous Nitric Oxide with Nitric Acid on Silica
822 Surfaces in the Presence of Water at Room Temperature, *J. Phys. Chem. A*, 105, 10339–10346,
823 <https://doi.org/10.1021/jp012330r>, 2001.

824 San Martini, F. M., Dunlea, E. J., Grutter, M., Onasch, T. B., Jayne, J. T., Canagaratna, M. R., Worsnop, D. R.,
825 Kolb, C. E., Shorter, J. H., Herndon, S. C., Zahniser, M. S., Ortega, J. M., McRae, G. J., Molina, L. T., and Molina,
826 M. J.: Implementation of a Markov Chain Monte Carlo method to inorganic aerosol modeling of observations
827 from the MCMA-2003 campaign Part I: Model description and application to the La Merced site,
828 *Atmospheric Chem. Phys.*, 6, 4867–4888, <https://doi.org/10.5194/acp-6-4867-2006>, 2006.

829 Scott, D. C., Herman, R. L., Webster, C. R., May, R. D., Flesch, G. J., and Moyer, E. J.: Airborne Laser Infrared
830 Absorption Spectrometer (ALIAS-II) for in situ atmospheric measurements of N₂O, CH₄, CO, HCl, and NO₂
831 from balloon or remotely piloted aircraft platforms, *Appl. Opt.*, 38, 4609–4622,
832 <https://doi.org/10.1364/AO.38.004609>, 1999.

833 Simpson, W. R., Brown, S. S., Saiz-Lopez, A., Thornton, J. A., and von Glasow, R.: Tropospheric Halogen
834 Chemistry: Sources, Cycling, and Impacts, *Chem. Rev.*, 115, 4035–4062, <https://doi.org/10.1021/cr5006638>,
835 2015.

836 Singh, H. B., Gregory, G. L., Anderson, B., Browell, E., Sachse, G. W., Davis, D. D., Crawford, J., Bradshaw, J.
837 D., Talbot, R., Blake, D. R., Thornton, D., Newell, R., and Merrill, J.: Low ozone in the marine boundary layer of
838 the tropical Pacific Ocean: Photochemical loss, chlorine atoms, and entrainment, *J. Geophys. Res. Atmospheres*,
839 101, 1907–1917, <https://doi.org/10.1029/95JD01028>, 1996.

840 Sumner, A. L., Menke, E. J., Dubowski, Y., Newberg, J. T., Penner, R. M., Hemminger, J. C., Wingen, L. M.,
841 Brauers, T., and Finlayson-Pitts, B. J.: The nature of water on surfaces of laboratory systems and implications for
842 heterogeneous chemistry in the troposphere, *Phys. Chem. Chem. Phys.*, 6, 604–613,
843 <https://doi.org/10.1039/B308125G>, 2004.

844 Tao, Y., VandenBoer, T. C., Veres, P. R., Warneke, C., de Gouw, J. A., Weber, R. J., Markovic, M. Z., Zhao, Y.,
845 Baker, K. R., Kelly, J. T., Murphy, J. G., Young, C. J., and Roberts, J. M.: Hydrogen Chloride (HCl) at Ground
846 Sites During CalNex 2010 and Insight Into Its Thermodynamic Properties, *J. Geophys. Res. Atmospheres*, 127,
847 e2021JD036062, <https://doi.org/10.1029/2021JD036062>, 2022.

848 Toth, R. A., Hunt, R. H., and Plyler, E. K.: Line strengths, line widths, and dipole moment function for HCl, *J.
849 Mol. Spectrosc.*, 35, 110–126, [https://doi.org/10.1016/0022-2852\(70\)90169-4](https://doi.org/10.1016/0022-2852(70)90169-4), 1970.

850 Tuckermann, M., Ackermann, R., Gölz, C., Lorenzen-Schmidt, H., Senne, T., Stutz, J., Trost, B., Unold, W., and
851 Platt, U.: DOAS-observation of halogen radical-catalysed arctic boundary layer ozone destruction during the
852 ARCTOC-campaigns 1995 and 1996 in Ny-Ålesund, Spitsbergen, *Tellus B Chem. Phys. Meteorol.*, 49, 533–555,
853 <https://doi.org/10.3402/tellusb.v49i5.16005>, 1997.

854 Veres, P., Roberts, J. M., Warneke, C., Welsh-Bon, D., Zahniser, M., Herndon, S., Fall, R., and de Gouw, J.:
855 Development of negative-ion proton-transfer chemical-ionization mass spectrometry (NI-PT-CIMS) for the
856 measurement of gas-phase organic acids in the atmosphere, *Int. J. Mass Spectrom.*, 274, 48–55,
857 <https://doi.org/10.1016/j.ijms.2008.04.032>, 2008.

858 Wang, X., Jacob, D. J., Eastham, S. D., Sulprizio, M. P., Zhu, L., Chen, Q., Alexander, B., Sherwen, T., Evans,
859 M. J., Lee, B. H., Haskins, J. D., Lopez-Hilfiker, F. D., Thornton, J. A., Huey, G. L., and Liao, H.: The role of
860 chlorine in global tropospheric chemistry, *Atmospheric Chem. Phys.*, 19, 3981–4003, <https://doi.org/10.5194/acp-19-3981-2019>, 2019.

862 Wang, X., Jacob, D. J., Downs, W., Zhai, S., Zhu, L., Shah, V., Holmes, C. D., Sherwen, T., Alexander, B., Evans,
863 M. J., Eastham, S. D., Neuman, J. A., Veres, P. R., Koenig, T. K., Volkamer, R., Huey, L. G., Bannan, T. J.,
864 Percival, C. J., Lee, B. H., and Thornton, J. A.: Global tropospheric halogen (Cl, Br, I) chemistry and its impact
865 on oxidants, *Atmospheric Chem. Phys.*, 21, 13973–13996, <https://doi.org/10.5194/acp-21-13973-2021>, 2021.

866 Watson, N.: Ammonia and Water Abundance Measurements from Los Gatos Research Ammonia Analyzer
867 Instrument at Manchester Air Quality Site 2019-22, *NERC EDS Cent. Environ. Data Anal.*,
868 <https://catalogue.ceda.ac.uk/uuid/5fc811f707f54415b129882a38889501>, 2022a.

869 Watson, N.: Nitrogen Dioxide Abundance Data from Teledyne Model T500U Instrument at the Manchester Air
870 Quality Site, NERC EDS Cent. Environ. Data Anal.,
871 <https://catalogue.ceda.ac.uk/uuid/f60761f3279042859e5c2902dfa0f2ef>, 2022b.

872 Watson, N.: NO and NO_y Abundance Data from Thermo Model 42i-Y NO_y Analyzer Instrument at the
873 Manchester Air Quality Site, NERC EDS Cent. Environ. Data Anal.,
874 <https://catalogue.ceda.ac.uk/uuid/1d58f2f5e7874e55a83ca57311dcfb9a>, 2022c.

875 Webster, C. R., May, R. D., Trimble, C. A., Chave, R. G., and Kendall, J.: Aircraft (ER-2) laser infrared absorption
876 spectrometer (ALIAS) for in-situ stratospheric measurements of HCl, N₂O, CH₄, NO₂, and HNO₃, *Appl. Opt.*, 33,
877 454–472, <https://doi.org/10.1364/AO.33.000454>, 1994.

878 Wilkerson, J., Sayres, D. S., Smith, J. B., Allen, N., Rivero, M., Greenberg, M., Martin, T., and Anderson, J. G.:
879 In situ observations of stratospheric HCl using three-mirror integrated cavity output spectroscopy, *Atmospheric
880 Meas. Tech. Discuss.*, 1–38, <https://doi.org/10.5194/amt-2021-6>, 2021.

881 Wingenter, O. W., Kubo, M. K., Blake, N. J., Smith Jr., T. W., Blake, D. R., and Rowland, F. S.: Hydrocarbon
882 and halocarbon measurements as photochemical and dynamical indicators of atmospheric hydroxyl, atomic
883 chlorine, and vertical mixing obtained during Lagrangian flights, *J. Geophys. Res. Atmospheres*, 101, 4331–4340,
884 <https://doi.org/10.1029/95JD02457>, 1996.

885 Yokelson, R. J., Christian, T. J., Bertschi, I. T., and Hao, W. M.: Evaluation of adsorption effects on measurements
886 of ammonia, acetic acid, and methanol, *J. Geophys. Res. Atmospheres*, 108,
887 <https://doi.org/10.1029/2003JD003549>, 2003.

888 Zahniser, M. S., Nelson, D. D., McManus, B., Kebabian, P. L., and Lloyd, D.: Measurement of trace gas fluxes
889 using tunable diode laser spectroscopy, *Philos. Trans. R. Soc. Lond. Ser. Phys. Eng. Sci.*, 351, 371–382,
890 <https://doi.org/10.1098/rsta.1995.0040>, 1995.

891 Zhang, B., Shen, H., Yun, X., Zhong, Q., Henderson, B. H., Wang, X., Shi, L., Gunthe, S. S., Huey, L. G., Tao,
892 S., Russell, A. G., and Liu, P.: Global Emissions of Hydrogen Chloride and Particulate Chloride from Continental
893 Sources, *Environ. Sci. Technol.*, 56, 3894–3904, <https://doi.org/10.1021/acs.est.1c05634>, 2022.

894